INTERNATIONAL JOURNAL FOR NUMERICAL METHODS IN ENGINEERING
Int. J. Numer. Meth. Engng 2004; **61**:2205–2238
Published online 18 October 2004 in Wiley InterScience (www.interscience.wiley.com). DOI: 10.1002/nme.1142

Constitutive model for quasi-static deformation of metallic sandwich cores

Zhenyu Xue and John W. Hutchinson*, †

Division of Engineering and Applied Sciences, Harvard University, Cambridge, MA 02138, U.S.A.

SUMMARY

All-metal sandwich construction holds promise for significant improvements in stiffness, strength and blast resistance for built-up plate structures. Analysis of the performance of sandwich plates under various loads, static and dynamic, requires modelling of face sheets and core with some fidelity. While it is possible to model full geometric details of the core for a few selected problems, this is unnecessary and unrealistic for larger complex structures under general loadings. In this paper, a continuum constitutive model is proposed as an alternative means of modelling the core. The constitutive model falls within the framework of a compressible rate-independent, anisotropic elastic–plastic solid. The general form of the model is presented, along with algorithmic aspects of its implementation in a finite element code, and selected problems are solved which benchmark the code against existing codes for limiting cases and which illustrate features specific to compressible cores. Three core geometries (pyramidal truss, folded plate, and square honeycomb) are considered in some detail. The validity of the approach is established by comparing numerical finite element simulations using the model with those obtained by a full three-dimensional meshing of the core geometry for each of the three types of cores for a clamped sandwich plate subject to uniform pressure load. Limitations of the model are also discussed. Copyright © 2004 John Wiley & Sons, Ltd.

KEY WORDS: sandwich plate; sandwich core; constitutive model; finite element method; plasticity

1. INTRODUCTION

Metallic sandwich structures, comprised of stiff face sheets and low-density core configurations, are now used as weight efficient structures [1, 2]. Recent attention has focused on the design of sandwich plate structures that are stiff, strong and effective against blast-type loads [3–5].

*Correspondence to: J. W. Hutchinson, Division of Engineering and Applied Sciences, Harvard University, Cambridge, MA 02138, U.S.A.
†E-mail: hutchinson@husm.harvard.edu

Contract/grant sponsor: ONR; contract/grant numbers: GG 10376-114934 and N00014-02-1-0700
Contract/grant sponsor: Division of Engineering and Applied Sciences, Harvard University

Received 24 October 2003
Revised 26 March 2004
Accepted 19 April 2004

All-metal construction is used in ship hulls and decks with structure ranging from sandwich plates to very thick double-hulls. The relative density of the cores (i.e. the ratio of volume of core material to the volume of core) in these sandwiches is very low, typically 5% or less. For certain types of analysis, these sandwich plates structures can be represented as conventional plates by using their effective bending and stretching stiffness. However, to capture the performance of such structures under loads that stress them to their limits, as in the case of collisions or blasts, it is essential to distinguish between the faces and core of the sandwich and to account for the geometry of the core and its interaction with the face sheets. This is particularly true in efforts to establish core designs that are most effective in collisions or blasts. A recent study made use of three-dimensional finite element analysis with full meshing of the core for three geometries (truss cores, folded plate cores and honeycomb cores) to explore the relative effectiveness of these cores under blast loads [3]. Full meshing of the cores was only feasible because the periodic nature of the sandwich plate considered made it possible to focus the analysis on a small repetitive sub-section of the structure using periodic boundary conditions. Problems involving more complex sandwich construction under general loads will be too large if detailed meshing of the core is attempted. Moreover, recent analytic work has indicated that reasonably accurate predictions for sandwich plate responses can be obtained without detailed characterization of the core as long as its energy absorbing capacities are correctly represented for the relevant modes of deformation [4].

An alternative approach to full meshing of core geometry is to model the core by a continuum constitutive law and fill the space between the faces with smeared out 'core material'. This approach can significantly reduce the size of the numerical problem, and, if carried out correctly, it should be able to accurately capture structural response for engineering purposes under many loading scenarios. Given the range of problems to which it is likely to be applied, the substitute constitutive relation will be required to reasonably replicate the elastic–plastic response of the core under several types of deformation including out-of-plane crushing, shearing and in-plane stretching.

The present paper presents a continuum constitutive model for metallic sandwich cores. The constitutive model falls within the framework of a compressible rate-independent, orthotropic elastic–plastic solid. Rate-dependence, whether from local inertial effects in the core or material-rate dependence, will influence structural response under high rate loads such as blasts. These effects will be incorporated into the model in subsequent work. The first half of this paper presents the model in general form, along with algorithmic aspects for its implementation in a finite element code, and benchmarks its performance in limiting cases against existing constitutive models. The second half specializes the constitutive model for three core geometries (pyramidal truss, folded plate, and square honeycomb). It then examines the validity of the approach by comparing numerical finite element simulations using the model with those obtained by a full three-dimensional meshing of the detailed core geometry for each of the three cores for a clamped sandwich plate deformed to large deformations by a uniform lateral pressure.

An example illustrating the type of constitutive law being sought here, and which is included as a special case of the present relation, is the Deshpande–Fleck constitutive model for metallic foams [6]. The model is an isotropic dilatational plasticity relation that employs a yield surface specified by

$$\hat{\sigma} = \sigma_Y^c \tag{1}$$

where $\hat{\sigma}$ is an *effective stress*, defined by

$$\hat{\sigma}^2 \equiv \frac{1}{1+(\alpha/3)^2}[\sigma_e^2 + \alpha^2 \sigma_m^2] \tag{2}$$

Here, $\sigma_e = \sqrt{3 s_{ij} s_{ij}/2}$ is the conventional effective stress with s_{ij} as the stress deviator, and $\sigma_m = \sigma_{kk}/3$ as the mean stress. The compressive yield stress of the core, σ_Y^c, is a prescribed function of the equivalent plastic strain fit to data taken under uniaxial compression. Normality of plastic flow is assumed. For metal foams, the parameter α is usually chosen to produce a specific 'plastic Poisson's ratio', $\nu_p = -\dot{\varepsilon}_{22}^p/\dot{\varepsilon}_{11}^p$, corresponding to uniaxial compression in the 1-direction:

$$\alpha = 3\left(\frac{1/2-\nu^p}{1+\nu^p}\right)^{1/2} \quad \text{or} \quad \nu_p = \frac{1/2-(\alpha/3)^2}{1+(\alpha/3)^2} \tag{3}$$

In the spirit of the present approach, this model was adopted by Xue and Hutchinson [5] as a core constitutive model for truss core sandwich plates subject to blast loads. In that study, the compressive yield strength, σ_Y^c, was matched to the corresponding crushing strength of the truss core, and the plastic Poisson's ratio, ν_p, was taken to be zero, motivated by the fact that the compressive behaviour of the truss core normal to the faces is essentially independent of the small strains occurring parallel to the faces. While this constitutive model of the core was able to reproduce certain aspects of the dynamic response of a truss core sandwich plate, it overestimated the contribution of the core to the in-plane stretching resistance at large deflections. A truss core has essentially no in-plane stretch resistance, which the isotropic foam model overestimates significantly. The constitutive model presented here will be able to capture both the anisotropy and compressibility of representative sandwich cores.

2. CONSTITUTIVE MODEL FOR METALLIC SANDWICH CORES

In this section, an anisotropic constitutive mode is developed for metallic sandwich cores. As emphasized in the introduction, many metallic sandwich core structures have low relative density, are highly compressible and exhibit anisotropic plastic behaviour, aspects which must be characterized by the constitutive model. In an application, the model must be able to replicate the stress–strain behaviour under the range of multi-axial stress histories that occur. The present model will be discussed relative to other types of models in the concluding section.

2.1. Orthotropic yield criterion for dilatational plasticity

We begin by stating the Hill criterion [7, 8] widely used for materials of that are incompressible and orthotropic with respect to the x_i axis. The yield criterion can be stated as

$$f = \sigma_e - \sigma_0 = 0 \tag{4}$$

where σ_0 is the effective yield stress and the effective stress, σ_e, is defined to be

$$\sigma_e = \sqrt{F(\sigma_y - \sigma_z)^2 + G(\sigma_z - \sigma_x)^2 + H(\sigma_x - \sigma_y)^2 + 2G\sigma_{yz}^2 + 2M\sigma_{zx}^2 + 2N\sigma_{xy}^2} \tag{5}$$

The dimensionless coefficients, F, G, H, L, M, N, determine the level of orthotropy and are usually obtained by fitting to data from multiple tests of the material. This yield function is independent of the hydrostatic, or mean stress. When the assumption of normality of plastic strain rate to the yield surface is invoked, the plastic strain gives rise to no volume change.

To account for compressibility of sandwich core, we extend Hill's criterion by retaining (4) and introducing a dependence of the effective stress on the mean stress by adding three normal stress terms:

$$\begin{aligned} 2\sigma_e^2 = {} & \alpha_{12}(\sigma_{11} - \sigma_{22})^2 + \alpha_{23}(\sigma_{22} - \sigma_{33})^2 + \alpha_{31}(\sigma_{33} - \sigma_{11})^2 \\ & + 6\alpha_{44}\sigma_{12}^2 + 6\alpha_{55}\sigma_{23}^2 + 6\alpha_{66}\sigma_{31}^2 + \alpha_{11}\sigma_{11}^2 + \alpha_{22}\sigma_{22}^2 + \alpha_{33}\sigma_{33}^2 \end{aligned} \tag{6}$$

The coefficients α_{11}, α_{22} and α_{33} create the dependence on the mean stress and, in conjunction with the assumption of normality, give rise to plastic volume change. The other coefficients are identical to those in the Hill criterion apart from numerical factors. Calibration of these coefficients against experimental data will be discusses in Section 2.5, along with some of the obvious limitations of the criterion such as the fact that it predicts yield to be independent of the sign of the stress tensor. In addition to reducing to the Hill criterion in the limit of plastic incompressibility, the criterion includes the Deshpande–Fleck formulation for compressible, isotropic metal foams if the coefficients of the effective stress are taken as

$$\begin{aligned} \alpha_{12} = \alpha_{23} = \alpha_{31} &= \frac{9 - 2\alpha^2}{9 + \alpha^2} \\ \alpha_{44} = \alpha_{55} = \alpha_{66} &= \frac{9}{9 + \alpha^2} \\ \alpha_{11} = \alpha_{22} = \alpha_{33} &= \frac{6\alpha^2}{9 + \alpha^2} \end{aligned} \tag{7}$$

where α is defined in (3).

2.2. Associated plastic flow rule

An associated plastic flow rule is adopted such that the plastic strain rate is assumed to be normal to the yield surface according to

$$\dot{\varepsilon}_{ij}^{p} = \dot{\lambda}\,\frac{\partial f}{\partial \sigma_{ij}} \tag{8}$$

where $\dot{\lambda}$ is the plastic strain-rate multiplier. An equivalent plastic strain rate $\dot{\varepsilon}_{ep}$ which is the plastic work rate conjugate to σ_e is defined such that

$$\dot{W} = \sigma_{ij}\dot{\varepsilon}_{ij}^{p} = \sigma_e \dot{\varepsilon}_{ep} \tag{9}$$

A straightforward relation between $\dot{\lambda}$ and $\dot{\varepsilon}_{\mathrm{ep}}$ can be obtained by substituting (8) into (9). Then, because f is a homogeneous function of order of the stress components, one has

$$\dot{\varepsilon}_{\mathrm{ep}} = \dot{\lambda} \frac{\sigma_{ij}}{\sigma_{\mathrm{e}}} \frac{\partial \sigma_{\mathrm{e}}}{\partial \sigma_{ij}} \equiv \dot{\lambda} \tag{10}$$

Thus, the flow rule (8) can be expressed as

$$\dot{\varepsilon}^{\mathrm{p}}_{ij} = \dot{\varepsilon}_{\mathrm{ep}} \frac{\partial f}{\partial \sigma_{ij}} \tag{11}$$

2.3. Strain hardening

The characterization of hardening for anisotropic materials such as the core structures of interest is far from straightforward if one hopes to account for widely different behaviour exhibited by the cores under different conditions of straining such as out-of-plane crushing and shear and in-plane stretching. In present paper, the simplest possible approach is adopted which we will call uniform hardening, similar to what is commonly done to characterize hardening based on the Hill criterion. Like isotropic hardening, uniform hardening preserves the shape of the yield surface, expanding it uniformly by making use of the effective stress (6) defined for the orthotropic material. Strain-rate sensitivity is not taken into account in the present model. It is assumed the effective yield stress can be expressed as a function of the equivalent plastic strain, $\varepsilon_{\mathrm{ep}} = \int \dot{\varepsilon}_{\mathrm{ep}}$, by

$$\sigma_0 = \sigma_0(\varepsilon_{\mathrm{ep}}) \tag{12}$$

where the plastic strain-rates are defined by (9) and (11). This function may be chosen to fit stress–strain behaviour of the core for one designated stress history as determined from either experimental data or theoretical simulation. The strain-hardening modulus, H, is

$$H = \mathrm{d}\sigma_0/\mathrm{d}\varepsilon_{\mathrm{ep}} \tag{13}$$

with $H > 0$ and $H < 0$ characterizing hardening and softening behaviour, respectively, and $H = 0$ describing perfectly plastic behaviour.

For applications involving significant out-of-plane crushing of the core, the best choice would fit (12) to data for uniaxial straining in compression in the out-of-plane direction. In applications where core shear is critical, the out-of-plane shear history would be the best choice. The accuracy to which the uniform hardening characterization reproduces other histories must be considered if those histories occur in a particular application, possibly limiting the utility of the model. Use of any of the currently available constitutive models for low-density core materials involves compromise in multi-axial stressing applications. For example, models that relate individual components of strain to corresponding components of stress as determined by single component stress–strain data [9] necessarily fail to account for well-known interactions due to multi-axial stressing. Compromises necessary in model choice will be summarized later.

2.4. Orthotropic elasticity

The plasticity of the core is supplemented by orthotropic linear elastic behaviour. In the axes of orthotropy, the elastic properties are specified by the nine ‘engineering constants’: three Young’s

moduli E_1, E_2, E_3; three independent Poisson's ratios ν_{12}, ν_{13}, ν_{23}; and three independent shear moduli G_{12}, G_{23}, and G_{31} such that

$$\begin{Bmatrix} \sigma_{11} \\ \sigma_{22} \\ \sigma_{32} \\ \sigma_{12} \\ \sigma_{23} \\ \sigma_{31} \end{Bmatrix} = \mathbf{C} \begin{Bmatrix} \varepsilon_{11} \\ \varepsilon_{22} \\ \varepsilon_{32} \\ \varepsilon_{12} \\ \varepsilon_{23} \\ \varepsilon_{31} \end{Bmatrix} = \begin{bmatrix} 1/E_1 & -\nu_{21}/E_2 & -\nu_{31}/E_3 & 0 & 0 & 0 \\ -\nu_{12}/E_1 & 1/E_2 & -\nu_{32}/E_3 & 0 & 0 & 0 \\ -\nu_{13}/E_1 & -\nu_{23}/E_2 & 1/E_3 & 0 & 0 & 0 \\ 0 & 0 & 0 & 1/G_{12} & 0 & 0 \\ 0 & 0 & 0 & 0 & 1/G_{23} & 0 \\ 0 & 0 & 0 & 0 & 0 & 1/G_{31} \end{bmatrix}^{-1} \begin{Bmatrix} \varepsilon_{11} \\ \varepsilon_{22} \\ \varepsilon_{32} \\ \varepsilon_{12} \\ \varepsilon_{23} \\ \varepsilon_{31} \end{Bmatrix} \tag{14}$$

Here, $\mathbf{C}$ is the elastic stiffness matrix; ν_{ij} is equal to the negative value of the ratio of the transverse strain in the j-direction and the strain in the i-direction when the material is elastically stressed in i-direction with $\nu_{ij}/E_i = \nu_{ji}/E_j$ such that ν_{ij} is not generally the same as ν_{ji}. Additionally, positive definiteness of $\mathbf{C}$ requires

$$\begin{cases} E_1, E_2, E_3, G_{12}, G_{23}, G_{31} > 0 \\ |\nu_{12}| < (E_1/E_2)^{1/2} \\ |\nu_{13}| < (E_1/E_3)^{1/2} \\ |\nu_{23}| < (E_2/E_3)^{1/2} \\ 1 - \nu_{12}\nu_{21} - \nu_{23}\nu_{32} - \nu_{31}\nu_{13} - 2\nu_{21}\nu_{32}\nu_{13} > 0 \end{cases} \tag{15}$$

2.5. *Calibration of coefficients α_{ij} and hardening function $\sigma_0(\varepsilon_{\mathrm{ep}})$*

Application of the constitutive model requires specification of eighteen coefficients and one hardening function: nine for elasticity (E_1, E_2, E_3, ν_{12}, ν_{13}, ν_{23}, G_{12}, G_{23}, G_{31}), nine for plasticity (α_{11}, α_{22}, α_{33}, α_{44}, α_{55}, α_{66}, α_{12}, α_{23}, α_{31}), and $\sigma_0(\varepsilon_{\mathrm{ep}})$. In principle, data from six sets of stress–strain histories are required to calibrate the model. Uniaxial stressing (tension or compression) along each of the axes of orthotropy provides the three Young moduli and three Poisson ratios, while three shear 'tests' provide the three shear moduli. Each of these sets of simple stressing data generates additional information needed for determining α_{ij} and $\sigma_0(\varepsilon_{\mathrm{ep}})$, as described below. As already noted, only one set of data can be used to specify $\sigma_0(\varepsilon_{\mathrm{ep}})$.

Rewrite the effective stress σ_{e} in the matrix/vector form as

$$\sigma_{\mathrm{e}} = \left(\tfrac{1}{2}\boldsymbol{\sigma}^{\mathrm{T}}\mathbf{P}\boldsymbol{\sigma}\right)^{1/2} \tag{16}$$

where, $\boldsymbol{\sigma} = [\sigma_{11}\ \sigma_{22}\ \sigma_{33}\ \sigma_{12}\ \sigma_{23}\ \sigma_{31}]^{\mathrm{T}}$; $\mathbf{P}$ is the plasticity matrix, which from (6) is

$$\mathbf{P} = \begin{bmatrix} \alpha_{12}+\alpha_{31}+\alpha_{11} & -\alpha_{12} & -\alpha_{31} & 0 & 0 & 0 \\ -\alpha_{12} & \alpha_{23}+\alpha_{12}+\alpha_{22} & -\alpha_{23} & 0 & 0 & 0 \\ -\alpha_{31} & -\alpha_{23} & \alpha_{31}+\alpha_{23}+\alpha_{33} & 0 & 0 & 0 \\ 0 & 0 & 0 & 6\alpha_{44} & 0 & 0 \\ 0 & 0 & 0 & 0 & 6\alpha_{55} & 0 \\ 0 & 0 & 0 & 0 & 0 & 6\alpha_{66} \end{bmatrix} \tag{17}$$

Then from (11), we have

$$\boldsymbol{\sigma} = \frac{2\sigma_{\mathrm{e}}}{\dot{\lambda}}\,\mathbf{P}^{-1}\dot{\boldsymbol{\varepsilon}}_{\mathrm{p}} \tag{18}$$

where $\dot{\boldsymbol{\varepsilon}}_{\mathrm{p}} = [\dot{\varepsilon}^{\mathrm{p}}_{11}\ \dot{\varepsilon}^{\mathrm{p}}_{22}\ \dot{\varepsilon}^{\mathrm{p}}_{33}\ 2\dot{\varepsilon}^{\mathrm{p}}_{12}\ 2\dot{\varepsilon}^{\mathrm{p}}_{23}\ 2\dot{\varepsilon}^{\mathrm{p}}_{31}]^{\mathrm{T}}$.[‡] Upon substituting (18) into (16) and simplifying, one obtains the explicit expression for the equivalent plastic strain rate

$$\dot{\varepsilon}_{\mathrm{ep}} = \sqrt{2}(\dot{\boldsymbol{\varepsilon}}^{\mathrm{T}}_{\mathrm{p}}\mathbf{P}^{-1}\dot{\boldsymbol{\varepsilon}}_{\mathrm{p}})^{1/2} \tag{19}$$

In what follows it is convenient to use an over-bar as special notation to signify the six simple stress histories having a single non-zero stress component in the axes of orthotropy. Thus, let $\bar{\sigma}_{ij}(\varepsilon_{\mathrm{ep}})$ denote the non-zero component in a simple history as predicted by the constitutive model at the effective plastic strain $\varepsilon_{\mathrm{ep}}$, i.e. $\bar{\sigma}_{11}$ indicates tensile stressing in the 1-direction while $\bar{\sigma}_{12}$ is reserved for a pure shear stress in the $(1, 2)$ axes, etc. Accordingly, for each of the six simple single-component stress histories, $\bar{\sigma}_{ij}(0)$ denotes that stress component at the onset of yield. One of the three uniaxial histories will be selected to determine $\sigma_0(\varepsilon_{\mathrm{ep}})$, and then $\sigma_0(0)$ denotes the value of the stress at yield for that history. Only positive $\bar{\sigma}_{ij}$ will be considered at this stage since the constitutive model predicts strictly anti-symmetric behaviour when the signs of the stress components are switched. The relation can be fit to either tensile or compressive data, but not both unless they are strictly anti-symmetric. Define initial yield stress ratios for the six simple histories according to $R_{ij} = \sigma_0(0)/\bar{\sigma}_{ij}(0)$. Since the yield surface has fixed shape and expands or contracts uniformly as $\varepsilon_{\mathrm{ep}}$ increases, the ratios $\sigma_0(\varepsilon_{\mathrm{ep}})/\bar{\sigma}_{ij}(\varepsilon_{\mathrm{ep}})$ do not change. In other words, the constitutive model implies the yield stress ratios for the six simple histories are fixed according to

$$R_{ij} = \sigma_0(0)/\bar{\sigma}_{ij}(0) = \sigma_0(\varepsilon_{\mathrm{ep}})/\bar{\sigma}_{ij}(\varepsilon_{\mathrm{ep}}) \tag{20}$$

For the three simple uniaxial histories, define six plastic 'Poisson ratios' such that for stressing in the x_i direction, $v^{\mathrm{p}}_{ij} = -\dot{\varepsilon}^{\mathrm{p}}_{jj}/\dot{\varepsilon}^{\mathrm{p}}_{ii}$ ($i \neq j$ and no summation on i or j). It follows from the fact that all coefficients, α_{ij}, in (6) are constants, that the plastic ratios are also independent

[‡]$\mathbf{P}$ is singular in the limit when the material is plastically incompressible. The algorithm for solving for the stresses in term of the strain-rates described in the appendix does not make use of the inverse of $\mathbf{P}$ and therefore the code developed applies whether or not the material is plastically incompressible.

of ε_{ep} for the present model. The following connections can be established directly from the constitutive model:

$$\alpha_{11} = 2R_{11}^2(1 - v_{12}^p - v_{13}^p), \quad \alpha_{22} = 2R_{22}^2(1 - v_{23}^p - v_{21}^p), \quad \alpha_{33} = 2R_{33}^2(1 - v_{31}^p - v_{32}^p)$$
$$6\alpha_{44} = 2R_{12}^2, \quad 6\alpha_{55} = 2R_{23}^2, \quad 6\alpha_{66} = 2R_{31}^2 \tag{21}$$
$$\alpha_{12} = 2R_{11}^2 v_{12}^p = 2R_{22}^2 v_{21}^p, \quad \alpha_{23} = 2R_{33}^2 v_{32}^p = 2R_{22}^2 v_{23}^p, \quad \alpha_{31} = 2R_{11}^2 v_{13}^p = 2R_{33}^2 v_{31}^p$$

These connections suggest several ways that the α_{ij} can be determined from material data. For example, suppose $\sigma_0(\varepsilon_{ep})$ is fit to data for uniaxial tension (or compression) in the 1-direction. If tension, then it is readily shown that $\varepsilon_{ep} = \varepsilon_{11}^p$, and, therefore, $\sigma_0(\varepsilon_{ep}) = \bar{\sigma}_{11}(\varepsilon_{11}^p)$. For stressing in the 1-direction the model reproduces the input stress–strain behaviour. Set the value of α_{44}, by taking R_{12} as the ratio of $\sigma_0(0)$ to the initial yield stress of the material for stressing in shear in the $(1, 2)$ axes, and similarly for (α_{55}, R_{23}) and (α_{66}, R_{31}). These choices ensure that initial yield of the material in each of the three simple shearing histories is reproduced by the model. Because $\sigma_0(\varepsilon_{ep}) = \bar{\sigma}_{11}(\varepsilon_{11}^p)$, $R_{11} = 1$. Further, identify R_{22} with the ratio of $\sigma_0(0)$ to the initial yield stress for stressing in the 2-direction, and similarly for R_{33} with stressing in the 3-direction. Again, these choices ensure that initial yield of the material is correctly reproduced for uniaxial stressing (tensile or compressive, depending on the choice) in the three directions of orthotropy. To determine the remaining α_{ij}, the plastic Poisson ratios must be specified, subject to the constraints of the last three equations in (21). There is some latitude in how this can be done. One possibility is to use uniaxial data from stressing in the 1-direction to identify v_{12}^p and v_{13}^p. Then, v_{21}^p and v_{31}^p are determined by (21). Finally, either v_{23}^p or v_{32}^p may be specified from respective sets of data, with the other determined by (21).

In summary, the process outlined above for identifying the coefficients of the effective stress and the hardening function ensures that the constitutive model reproduces initial yield of the material for all six of the simple stress histories. Furthermore, it reproduces the stress–strain curve for the history used to define the hardening behaviour and has constant Poisson ratios governing the plastic strain components that can be chosen to approximate behaviour for that history. Because uniform hardening is invoked, the stress–strain curve for each of the simple histories will have the same shape as that of the history used in setting the hardening function. As previously emphasized, this is a limitation of the model that must be considered for each application, as is the fact that the model predicts hardening to be independent of the sign of the stress. A combination of analytical solutions and finite element analysis will be employed to illustrate the identification process for three types of cores. Alternatively, experimental stress–strain data could also be used in calibrating the constitutive model.

The above constitutive model for sandwich core has been implemented into ABAQUS/Standard [10] through its UMAT subroutine interface. In the UMAT code, we adopt the backward-Euler return algorithm, the details of which are introduced in appendix.

3. NUMERICAL EXAMPLES

Problems have been solved with the implemented finite element code, in one case to benchmark the code and in the others to highlight behaviour unique to compressible, anisotropic

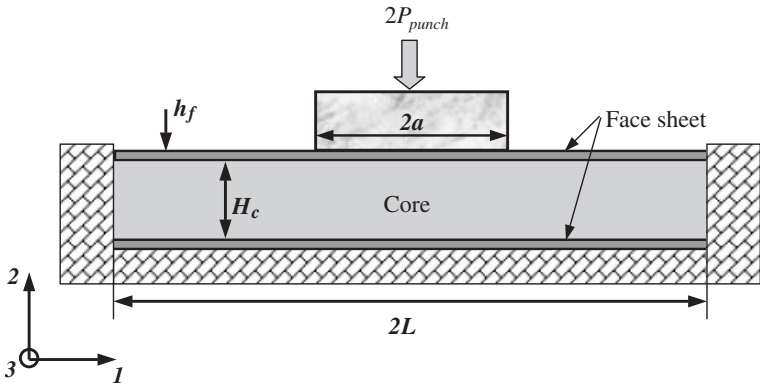

Figure 1. Schematic diagram of the indentation test of a sandwich plate.

cores. For the first problem, indentation of a sandwich plate with a soft core is considered for three constitutive characterizations of the core, each of which is fit to the same stress–strain curve governing uniaxial compression in the direction of indentation. The second problem is the bending under uniform pressure of a clamped–clamped sandwich plate whose core is represented by both the isotropic foam model and the present model with distinct anisotropy.

3.1. Indentation of a rigidly supported sandwich plate

As sketched in Figure 1, a section of sandwich plate of width $2L$ is constrained to undergo plane strain deformations. It has core thickness H_c, face sheets of equal thickness h_f, and is fully clamped along its sides. The plate is indented on the top surface by a rigid flat-bottom punch with length $2a$. For the specific example employed in the calculations, $a/L = 0.4$, $h_f/L = 0.008$, $H_c/L = 0.1$. The face sheets are made from 304 stainless steel. A piecewise function has been fit to the elastic–plastic tensile behaviour of the material [11] giving

$$\sigma = \begin{cases} E\varepsilon, & \varepsilon \leqslant 0.002 \\ \sigma_Y(\varepsilon/0.002)^N, & \varepsilon > 0.002 \end{cases} \tag{22}$$

with Young's modulus $E = 200\,\text{GPa}$; Poisson's ratio $\nu = 0.3$; initial tensile yield stress of the face plate $\sigma_Y = 205\,\text{MPa}$, strain hardening exponent $N = 0.17$ and density $\rho = 8000\,\text{kg/m}^3$. Isotropic hardening flow theory is employed to model the plastic behaviour of the face sheets based on the Mises yield criterion.

The problem will be solved for three constitutive models characterizing the core, each of which will be fit to the same uniaxial compression curve but will otherwise have distinct multiaxial behaviour. The axes of orthotropy are those shown in Figure 1 with the 2-axis as the indentation direction and the 3-axis in the direction of plane strain constraint. To motivate the material constants, imagine a core with symmetry similar to a square honeycomb. We take

elastic constants in all three cases to be

$$\begin{aligned} E_{11} &= E_{33} = 2\,\text{GPa}, \quad E_{22} = 4\,\text{GPa} \\ G_{12} &= G_{23} = 0.8\,\text{GPa}, \quad G_{13} = 0.008\,\text{GPa} \\ \nu_{12} &= \nu_{13} = \nu_{23} = 0 \end{aligned} \tag{23}$$

The compressive strain-hardening law for the core is taken to be

$$\sigma_0(\varepsilon_{\text{ep}}) = \sigma_0(0) + H\varepsilon_{\text{ep}}, \quad 0 \leqslant \varepsilon_{\text{ep}} \tag{24}$$

with initial yield stress $\sigma_0(0) = 4\,\text{MPa}$ and strain-hardening rate $H = 4\,\text{MPa}$. The core material is very soft compared to the face sheets since $\sigma_0(0)/\sigma_Y = 0.0195$.

The first model employed is Hill's model representing a *plastically incompressible core*. In addition to $\bar{\sigma}_{22}(0) = 4\,\text{MPa}$, the initial yield stresses are taken to be: $\bar{\sigma}_{11}(0) = \bar{\sigma}_{22}(0) = 2\,\text{MPa}$, $\bar{\sigma}_{12}(0) = \bar{\sigma}_{23}(0) = 1.25\text{MPa}$ and $\bar{\sigma}_{13}(0) = 0.025\text{MPa}$. This fully prescribes the Hill yield surface when the effective stress–strain curve is required to reduce to (24) for uniaxial stressing in the 2-direction. Normality provides the plastic Poisson ratios as $\nu_{12}^{\text{p}} = 0.125$, $\nu_{13}^{\text{p}} = 0.875$ and $\nu_{13}^{\text{p}} = 0.5$. This model is a limiting case of the present yield condition (6) giving

$$\alpha_{12} = \alpha_{23} = 1, \quad \alpha_{31} = 7, \quad \alpha_{44} = \alpha_{55} = 3.41, \quad \alpha_{66} = 8533, \quad \alpha_{11} = \alpha_{22} = \alpha_{33} = 0 \tag{25}$$

The second model considered is the isotropic foam criterion (2) representing a highly compressible core. In this case, the model is again fit to the uniaxial stress–strain relation (24) characterizing behaviour in the 2-direction. In addition, the plastic Poisson's ratio in (3) is taken to be $\nu_{\text{p}} = 0$ ($\alpha = 3/\sqrt{2}$). This fully specifies the foam model, which, again, is a special case (6) of the present model with

$$\alpha_{11} = \alpha_{22} = \alpha_{33} = 2, \quad \alpha_{12} = \alpha_{23} = \alpha_{31} = 0, \quad \alpha_{44} = \alpha_{55} = \alpha_{66} = 2/3 \tag{26}$$

The third model employs the present yield surface (6) for a *plastically compressible anisotropic core* that has precisely the same initial yield stresses for the six simple histories as for the Hill Model (i.e. $\bar{\sigma}_{22}(0) = 4\,\text{MPa}$, $\bar{\sigma}_{11}(0) = \bar{\sigma}_{22}(0) = 2\,\text{MPa}$, $\bar{\sigma}_{12}(0) = \bar{\sigma}_{23}(0) = 1.25\,\text{MPa}$ and $\bar{\sigma}_{13}(0) = 0.025\,\text{MPa}$). In addition, we require the following plastic Poisson ratios to be zero: $\nu_{12}^{\text{p}} = \nu_{13}^{\text{p}} = \nu_{23}^{\text{p}} = 0$. By (21), it then follows that all six plastic Poisson ratios are zero, consistent with the idea that the highly open core structure results in small transverse strains for uniaxial stressing in any direction. For this model

$$\alpha_{11} = \alpha_{33} = 8, \quad \alpha_{22} = 2, \quad \alpha_{44} = \alpha_{55} = 3.41, \quad \alpha_{66} = 8533, \quad \alpha_{12} = \alpha_{23} = \alpha_{31} = 0 \tag{27}$$

In summary, all three constitutive models are fit to the same stress–strain curve for uniaxial compression in the 2-direction perpendicular to the plane of the plate. Moreover, the incompressible Hill Model and the compressible version of the present anisotropic model share identical initial yield stresses for all six simple stress histories. Significant behavioural differences will be evident in the numerical examples discussed next.

The two-dimensional plane-strain problem is meshed with a rectangular grid shown in the deformed state in Figure 2. Symmetry permits half of the structure to be considered. The finite element model consists of a rigid indenter and a deformable sandwich plate modelled with 4-node plane-strain elements with reduced integration in ABAQUS/Standard. It is assumed that

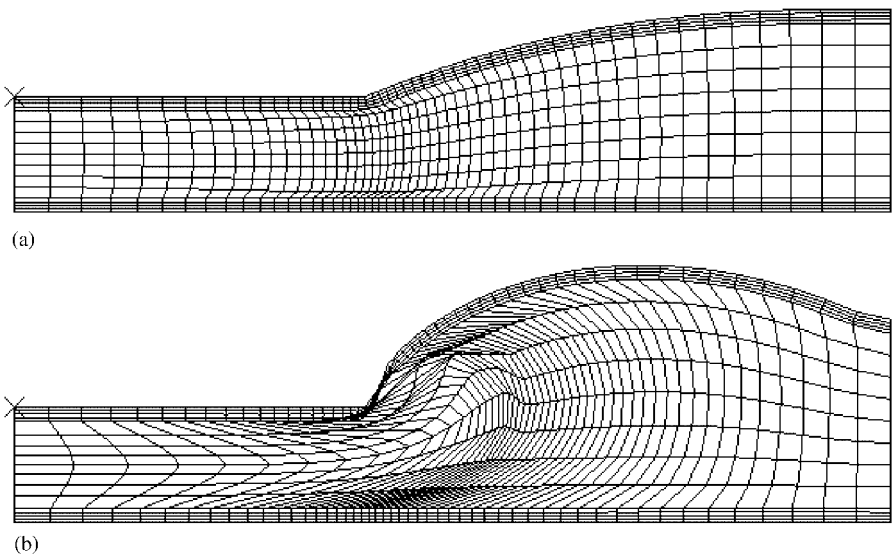

Figure 2. (a) The deformed configuration of the mesh for the indentation test of sandwich plate where the yield behaviour of the core is modelled by the present model for a plastically compressible core; and (b) The deformed configuration of the mesh for the indentation test of sandwich plate where the yield behaviour of the core is modelled by Hill's model with an incompressible core. Both (a) and (b) are fit to the same uniaxial behaviour for compression in the direction of indentation.

the rigid indenter is bonded to the top surface of the upper face sheet and that the indenter moves only in the vertical direction. The bottom surface of the lower face sheet and the edges of the sandwich plate are each imagined to be bonded to a rigid container such that the nodes on those surfaces do not move. Along the symmetry line at the centre, the nodes are constrained to move vertically. The computations are carried out within a finite strain framework using an updated Lagrangian formulation. The stresses and strains in the constitutive relations detailed above are interpreted to be true stresses and strains.

The load-deflection response for each of the three constitutive models is plotted in Figure 3. Although the uniaxial compressive stress–strain behaviour of the three core materials is the same in the direction perpendicular to the plate, the core modelled by the Hill relation offers significantly greater resistance to indentation than the other two cores due to its inability to undergo plastic volume change. The difference between the deformation fields is evident in Figure 2 corresponding to a moderately deep indentation, $\delta_{\text{punch}}/H_{\text{c}} = 0.47$. Incompressibility forces material to flow out from under the indenter and form a bulge (Figure 2(b)), while nearly all the deformation of the compressible material is confined to the region under the indenter (Figure 2(a)) for the case of the compressible core modelled by the present anisotropic yield criterion. A large hydrostatic compression forms under the indenter when the core is incompressible causing the elevation of the indenter load and squeezing core material out from under the indenter. This type of response can also be compared with the classical Hill solution for punch indentation into a rigid-plastic semi-space in plane strain status $P_{\text{punch}} = (2+\pi)a\sigma_0(0)$ [7, 12]. At the same time the one-dimensional model of punch indentation on a compressible

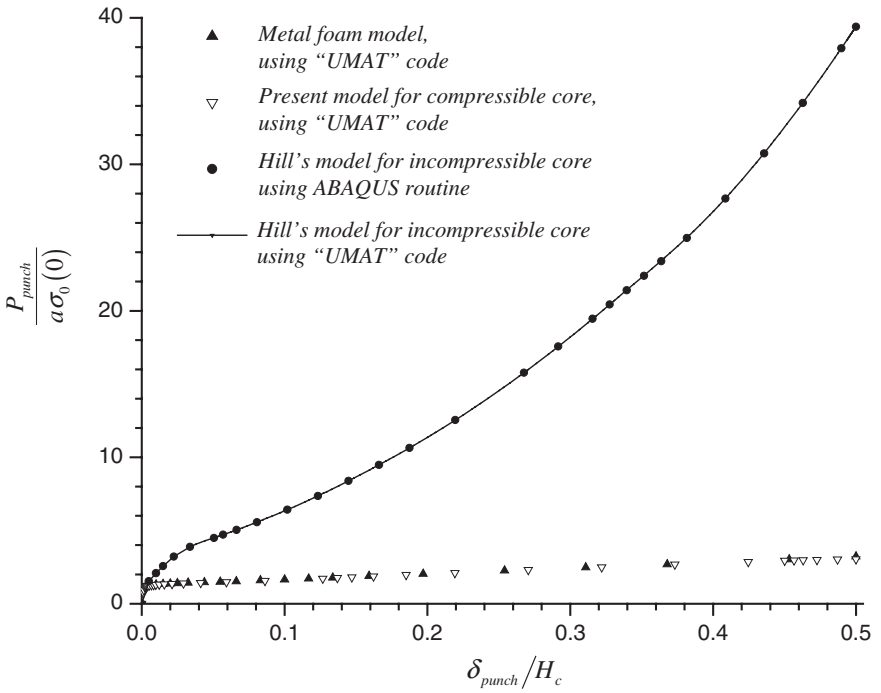

Figure 3. Force–displacement responses of the indenter predicted for various core constitutive models; P_{punch} is punch force per unit width for the half model; δ_{punch} is the deflection of the punch.

sandwich core gives $P_{\text{punch}} = a\sigma_0(0)$, neglecting the influence of the thin face sheet. Thus, the ratio between the incompressible and compressible solution is of the order of 5, which corresponds well to the relative position of two sets of curves shown in Figure 3. The state of stress under the indenter for the two compressible core materials, the anisotropic model and the isotropic foam model, is dominantly uniaxial compression with relatively little lateral plastic expansion. Since both material models have been fitted to the same compressive stress–strain curve, the load-deflection behaviours for the two compressible cores are almost identical.

As already emphasized, the classical Hill model for anisotropic, incompressible plasticity is included as a limiting case of the present model, and the UMAT module developed for the present model was used to compute all the results just discussed. The problem for the core described by the Hill model was re-solved using the same mesh with the Hill constitutive model for incompressible plastic flow as incorporated in the commercial version of ABAQUS. Results from the commercial ABAQUS constitutive code are shown as solid points in Figure 3, and it can be seen that they are essentially identical to the results obtained from the material subroutine developed for the present constitutive model. Run times using the present UMAT module compare closely with those using the commercial module. In addition, the problems were rerun with a finer mesh, and the load-displacement behaviour of the punch seen in Figure 3 remained essentially unchanged implying that the mesh shown is adequate to predict overall behaviour.

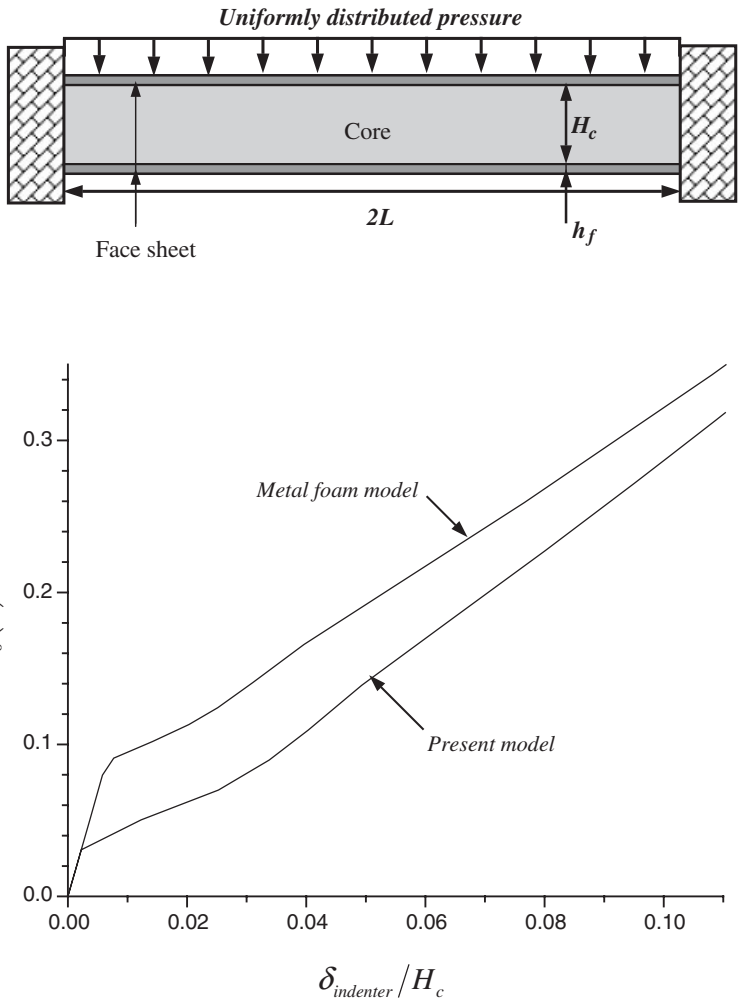

Figure 4. Pressure–deflection responses of clamped sandwich plates for cores represented by the metal foam model and the present core model. The initial yield stress in shear for the foam model is more that twice that of the present model in this case.

3.2. Deformation of a clamped sandwich beam under uniform pressure

As noted above, the similar indentation responses of the indented sandwich plate with the foam metal core and that with the compressible anisotropic core is due to the fact that both constitutive models have been fit to the same compressive stress–strain curve for crushing and both give rise to a stress state under the indenter that is dominantly uniaxial compression. The problem considered in this section involves both compression and shearing of the core, such that the role of the anisotropic strength of the core will become evident.

A clamped–clamped sandwich beam subject to uniform pressure has the geometry shown in Figure 4. The beam is a plate that is considered to be infinite in extent in the direction

perpendicular to the cross-section shown, and it is analysed as a plane strain problem using ABAQUS with the present UMAT material module. The stainless steel face sheets are again characterized by (22). The two compressible core materials introduced in the previous subsection will be considered in this comparison: the isotropic foam core model with (26) and the new anisotropic plasticity model with (27). Elastic moduli (23) are employed again for the core. Furthermore, as in the previous examples, we fit each relation to reproduce the same uniaxial stress–strain curve for uniaxial stressing perpendicular to the plane of the plate with an initial yield strength of 4 MPa and the hardening relation (24). The geometry is fixed with $H_c/L = 0.1$ and $h_f/H_c = 0.08$.

A plot of pressure versus deflection of the top face sheet at the centre of the beam, δ, is shown for each of the two sandwich plates in Figure 4. The substantially higher strength of the sandwich with the foam core relative to that with the anisotropic core sandwich shortly after overall yield is attributed to higher shear strength of the foam core. By (2), the initial yield strength in shear for the isotropic foam core is $\bar{\sigma}_{12}(0) = 4/\sqrt{2}\,\text{MPa} = 2.83\,\text{MPa}$, while the corresponding initial shear strength of the anisotropic core has been taken as $\bar{\sigma}_{12}(0) = 1.25\,\text{MPa}$. It is readily shown that the bending strength of the core contributes no more that 5% of the total bending strength of the beam for these examples. Thus, the fact that the initial in-plane stretching strength of the foam core (4 MPa) is also greater than that of the anisotropic core (2 MPa) is not an important factor in the difference in the behaviours seen in Figure 4. In-plane stretching strength of the core becomes important at larger deflections, when overall stretching of both faces and the core occurs. The example in Figure 4 illustrates how anisotropic yielding of the core can have a large influence on the behaviour of a sandwich plate.

4. SIMULATIONS OF CORE RESPONSE FOR BASIC HISTORIES

The second half of the paper elaborates the constitutive model for three core geometries: pyramidal truss, folded plate, and square honeycomb. For each of these core geometries, a combination of analytical and finite element solutions will be used to determine its response under the six simple stressing histories, $\bar{\sigma}_{ij}(\varepsilon_{ep})$. Then, the parameters of the constitutive model will be chosen to reproduce the six initial yield stresses, and the hardening function will be chosen to reproduce or approximate one of the six simple stress histories. The core constitutive model will then be used to represent the core of a clamped sandwich plate in a plane strain, finite element simulation of the deflection under a quasi-static uniform load. The validity of this approach is assessed by comparing deflections so obtained with those from a numerical finite element simulation using a full three-dimensional meshing of the detailed core geometry of the sandwich plate. The comparison is carried out for each of the three core geometries providing insight into the advantages and limitations of representing the core by a continuum constitutive model. For the plate with a square honeycomb core, further calculations have been performed making a similar comparison of results for a uniform impulsive load.

The three core geometries are shown in Figure 5: square honeycomb (Figure 5(a)), pyramidal truss (Figure 5(b)) and folded plate (Figure 5(c)), sometimes referred to as a corrugated plate core. The three core configurations are periodic in the lengthwise direction of the plate, as illustrated by sections of the plates shown in the deformed state in Figure 6. Periodicity is

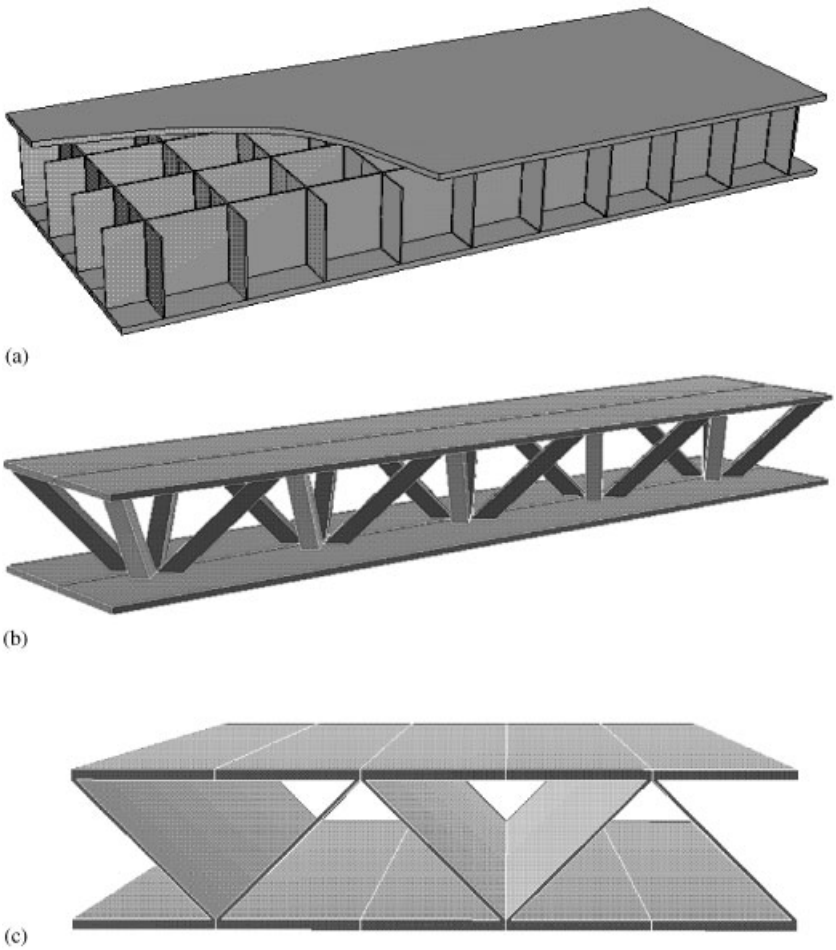

Figure 5. (a) Sandwich plate with square honeycomb core geometry; (b) sandwich plate with pyramidal truss core geometry; and (c) sandwich plate with folded plate core geometry.

exploited in the process of computing the response of the core for the six fundamental stressing histories, $\bar{\sigma}_{ij}(\varepsilon_{\text{ep}})$. Periodic boundary conditions are imposed on a unit cell of the core consistent with each history. The detailed analysis of the 'micro' behaviour of the core accounts for finite rotations and large plastic strains and it captures features such as plastic bucking and local necking of the core trusses or webs. Thus, the calculations carried out for obtaining the input to the continuum constitutive mode also provide valuable insight into the behaviour of the core under different modes of stressing.

The objective in this section is to determine the six histories, $\bar{\sigma}_{ij}(\varepsilon_{\text{ep}})$, together with the relevant plastic Poisson ratios, for each of the three core geometries. This information will then be used to calibrate the continuum constitutive model for the each of the cores.

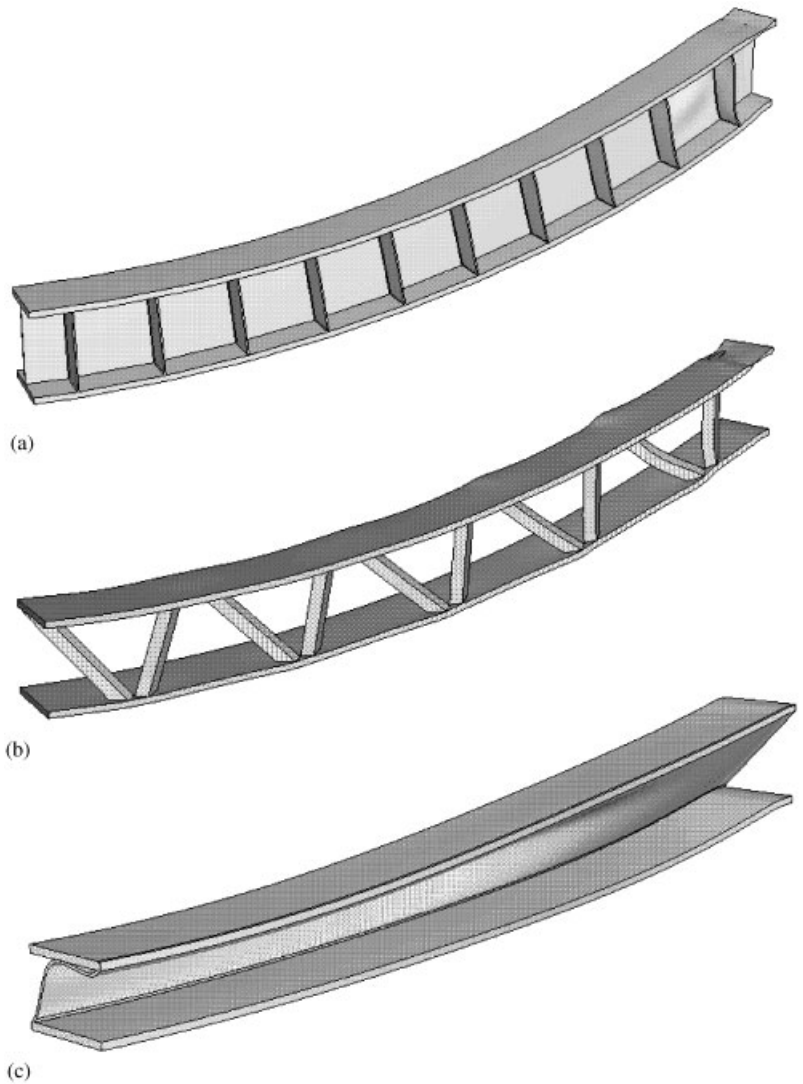

Figure 6. (a) Deformed configuration of the mesh for square honeycomb core sandwich plate under uniformly distributed pressure load; (b) deformed configuration of the mesh for pyramidal truss core sandwich plate under uniformly distributed pressure load; and (c) deformed mesh for folded plate core sandwich plate under uniformly distributed pressure load.

All components of the sandwich plates, faces and core, will be assumed to be made from 304 stainless steel (22). At the local scale the material is assumed to be characterized by flow theory with isotropic hardening based on the Mises yield criterion. For future reference it is noted that the shear modulus and initial shear strength of the material are $G = E/2(1 + \nu) = 76.92$ GPa and $\tau_Y = \sigma_Y/\sqrt{3} = 118.4$ MPa, respectively.

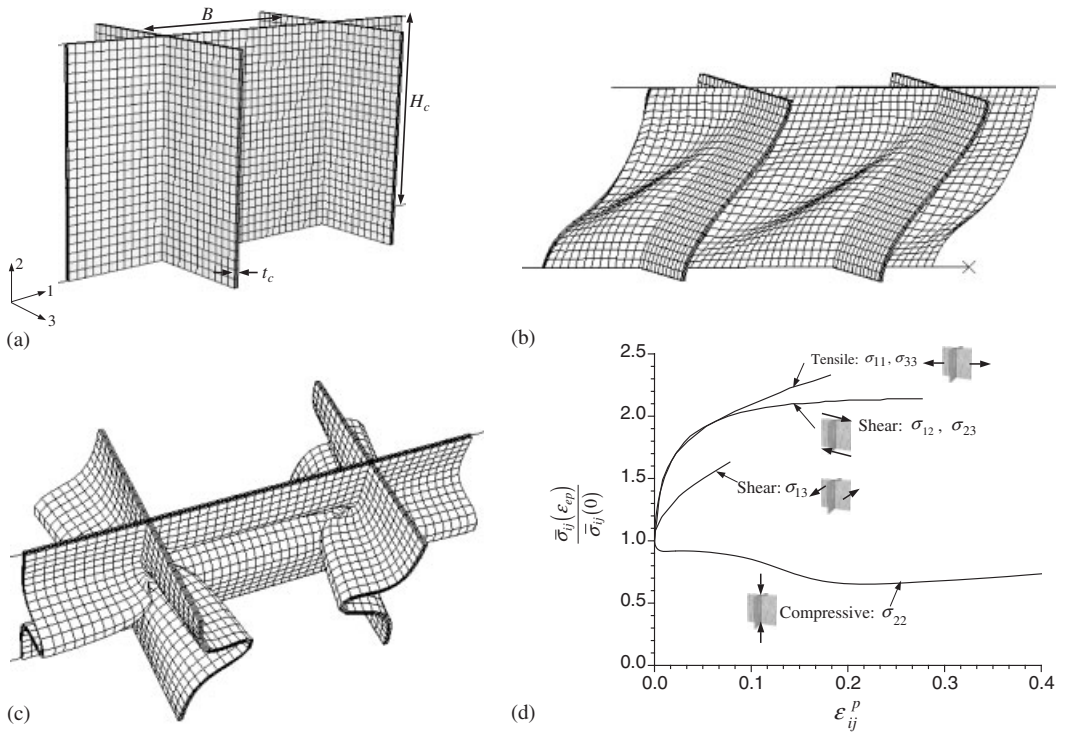

Figure 7. (a) Finite element model of a unit core cell for square honeycomb core geometry; (b) deformed configuration of the mesh showing shear buckling of the web for square honeycomb core; (c) deformed configuration of the mesh showing compressive buckling of the web for square honeycomb core; and (d) normalized stress–plastic strain relationships for square honeycomb core. (For each of the basic histories the horizontal axis is the respective strain component $\varepsilon_{ij}^{\mathrm{p}}$.)

4.1. Square honeycomb core

The sandwich plate with square honeycomb core geometry is sketched in Figure 5(a). A unit cell of the square honeycomb core is configured as shown in Figure 7(a) along with the coordinate system used to define the anisotropy. The height of the core is H_{c}, and the wall thickness of the core webs is t_{c}. The width of core web is B. The relative density of core, $\bar{\rho}_{\mathrm{c}}$, defined as the ratio of average density of the core to the density of material, ρ_{c}/ρ, (or, equivalently, as volume of material in the core to the volume of the core) can be expressed in terms as

$$\bar{\rho}_{\mathrm{c}} = 2\,\frac{t_{\mathrm{c}}}{B} - \left(\frac{t_{\mathrm{c}}}{B}\right)^2 \tag{28}$$

For the numerical examples studied in this paper, the geometry of square honeycomb core has $H_{\mathrm{c}}/B = 1$ and $t_{\mathrm{c}}/B = 0.02$ corresponding to $\bar{\rho}_{\mathrm{c}} = 0.04$. The core webs are taken as welded, i.e. clamped, to the face sheets, such that the deformation of the square web elements is significantly constrained by the face sheets. In this subsection, the first step will be to

obtain estimates of some of the core properties from simple theoretical analyses. The second step entails combinations of simple estimates and detailed three-dimensional finite element simulations of the core to more precisely capture its behaviour under the six basic histories.

4.1.1. Analytical estimates. The initial yield stresses of the core are readily estimated. For example, the average stress in the webs of the square honeycomb core when it is subject to an overall uniaxial stress σ in the 2-direction is $\bar{\sigma}_{22} = \bar{\rho}_c \sigma$. Thus, the initial yield stress for the core for this basic stress history is $\bar{\sigma}_{22}(0) = \bar{\rho}_c \sigma_Y$. Similar estimates for the other stress histories lead to

$$\bar{\sigma}_{11}(0) = \bar{\sigma}_{33}(0) \approx \tfrac{1}{2}\,\bar{\rho}_c \sigma_Y = 4.1\,\text{MPa}, \quad \bar{\sigma}_{22}(0) = \bar{\rho}_c \sigma_Y = 8.2\,\text{MPa} \tag{29a}$$

$$\bar{\sigma}_{12}(0) = \bar{\sigma}_{23}(0) \approx \tfrac{1}{2}\,\bar{\rho}_c \tau_Y = 2.367\,\text{MPa} \tag{29b}$$

where terms of relative order t_c/B have been neglected and numerical values are displayed for the specific example under consideration. In a similar way, the elastic moduli can be estimated giving

$$E_1 = E_3 \approx \tfrac{1}{2}\,\bar{\rho}_c E = 4\,\text{GPa}, \quad E_2 = \bar{\rho}_c E = 8\,\text{GPa} \tag{30a}$$

$$G_{12} = G_{23} \approx \tfrac{1}{2}\,\bar{\rho}_c G = 1.54\,\text{GPa} \tag{30b}$$

The yield strength and modulus of the square honeycomb core in the crushing direction are twice the corresponding in-plane quantities. The in-plane shear strength and elastic shear modulus are exceeding low and will be presented later; they are unimportant since the face sheets supply essentially all the in-plane shear strength and stiffness.

Next, all the Poisson ratios of the core are set to zero. This approximation is inconsequential in the elastic range since it is primarily the out-of-plane shear moduli that are important for the shear stiffness of the plates and these do not depend on Poisson ratios. Setting the plastic Poisson ratios to zero is a good approximation since the highly open structure of the core generally results in relatively small transverse stresses under uniaxial straining. For example, a square honeycomb welded to face sheets and crushed in the 2-direction induces relatively small transverse stress such that there is little distinction between uniaxial straining and uniaxial stressing. Thus, as an approximation, we take

$$\nu_{12} = \nu_{21} = \nu_{13} = \nu_{31} = \nu_{23} = \nu_{32} = 0 \tag{31a}$$

and

$$\nu^p_{12} = \nu^p_{21} = \nu^p_{13} = \nu^p_{31} = \nu^p_{23} = \nu^p_{32} = 0 \tag{31b}$$

These approximations simplify the task of determining the coefficients of the yield function, as discussed in the next sub-section. From (21), they imply $\alpha_{12} = \alpha_{23} = \alpha_{31} = 0$.

4.1.2. Finite element modelling of a unit core cell. Three-dimensional finite element modelling of the unit core cell is now used to simulate its force–displacement responses for several of the six basic stress histories. The finite element simulations are performed using

ABAQUS/Standard [10]. Recall that only one of the basic histories can be chosen to establish the hardening function, $\sigma_0(\varepsilon_{ep})$, of the core constitutive model. By presenting all six histories, we provide insight on how well one choice for the hardening function will represent the others.

The unit core cell is shown in Figure 7(a). It is fully meshed with eight-node linear brick elements with reduced integration. Rigid plates are bounded to top and bottom surfaces. The bottom plate is fixed. Symmetry dictates that the roles of the 1- and 3-direction can be interchanged. In computing the response to compressive stressing in the 2-direction, the lower plate is fixed and upper plate is displaced in the negative 2-direction. A small initial geometric imperfection (a transverse deflection that is 1% of the wall thickness) has been introduced to trigger the buckling response of core webs. The force–displacement response of the calculation gives the nominal, or engineering, stress and strain rate, $(\bar{\sigma}_{22})_{nom}$ and $(\dot{\bar{\varepsilon}}^{p}_{22})_{nom}$; these are converted to true stress $\bar{\sigma}_{22}$ and logarithmic plastic strain rate $\dot{\bar{\varepsilon}}^{p}_{22}$. The effective plastic strain rate is given by $\dot{\varepsilon}_{ep} = \sqrt{2/\alpha_{22}}|\dot{\bar{\varepsilon}}^{p}_{22}|$. In those instances when we choose the crushing history to fit the hardening function (i.e. $\sigma_0(\varepsilon_{ep}) = \bar{\sigma}_{22}(\varepsilon_{ep})$), $\sigma_0(0) = \bar{\sigma}_{22}(0)$, $\alpha_{22} = 2$ and $\dot{\varepsilon}_{ep} = |\dot{\bar{\varepsilon}}^{p}_{22}|$.[§] In other instances the hardening function will be fit to the shear history ($\sigma_0(\varepsilon_{ep}) = \bar{\sigma}_{12}(\varepsilon_{ep})$).

Strictly speaking, the core history modelled in Figure 7(a) with rigid plates attached at the top and bottom is uniaxial straining *not* uniaxial stressing. However, for the reasons mentioned earlier, it is expected there will be little difference between the two histories. The transverse stresses computed by averaging the tractions on the vertical edges of the webs are very small compared to $\bar{\sigma}_{22}$. Since the behaviour of the core attached to the face sheets is sought, the faces must be included in the simulation. For example, the faces provide significant support to the core webs where they are joined, and it would not be meaningful to attempt to assess the core response with any model that did not account for this support. For histories in which the face sheets contribute to either the stress or the strain in the overall response, those contributions must be 'subtracted off' in generating the result attributed to the core. Such steps are inherent to the approximation involved in modelling the core with a continuum constitutive relation.

Employing the uniaxial straining history to generate $\bar{\sigma}_{22}(\varepsilon_{ep})$ is fully consistent with the approximation adopted that all the Poisson ratio quantities are zero. An alternative procedure would compute the transverse stress generated for the history and strictly fit the constitutive model to the data so generated. That procedure would be considerably more difficult to carry out but it seems unlikely that the outcome would be much different. Yet another alternative would work with single component plastic strain histories rather that single component stress histories [13]. The complication associated with this approach is that histories with single plastic strain components, as opposed to a single total strain component, are not readily generated. Generally, both the present procedure and the parallel procedure in Reference [13] involve some level of approximation in identifying the coefficients and hardening function of the constitutive law. Depending on the particular core and the mode of deformation, one procedure may have advantages over the other, but in most instances, such as the cores studied here, both methods are expected to be effective and to yield comparable results.

The relation between $\bar{\sigma}_{22}$ and ε^{p}_{22} for crushing of the core is displayed in Figure 7(d) where $\bar{\sigma}_{22}(0)$ in (29a) is used as the normalizing factor. The material properties and relative density

[§]Although the stress σ_{22} in the crushing history is negative, each of the basic stress histories will be presented as being positive, with no loss in generality, because the constitutive law is strictly anti-symmetric in the relation between stress and strain. Specifically, $\bar{\sigma}_{22}$ will be taken as positive in the discussion.

of the core are such that there is little separation between elastic buckling and plastic yielding. Plastic buckling begins almost simultaneous with the onset of yielding. The crushing strength of the core falls gradually as deformation proceeds. By varying the choice of initial imperfection, several modes of buckling can be triggered having symmetry, or anti-symmetry, with respect to the original planes of the webs in the unit cell as discussed in References [14, 15]. The curve in Figure 7(d) has the mode form shown in Figure 7(c) which gave the lowest crushing curve of the modes analysed for this specific case.

The calculated result for in-plane tension, $\bar{\sigma}_{11}(\varepsilon_{11}^{\mathrm{p}})/\bar{\sigma}_{11}(0)$, is also plotted in Figure 7(d) where $\bar{\sigma}_{11}(0)$ is given by (29a). Over the range plotted, the curve is essentially the uniaxial stress–strain curve of the material. Necking of the web sets in at the point where the curve is terminated in Figure 6(b). Were the curve continued, $\bar{\sigma}_{11}(\varepsilon_{11}^{\mathrm{p}})$ would decrease, but gradually because of the constraining effect of the face sheets on the necking mode. Results at larger strains have not been presented since a sandwich plate will seldom experience larger in-plane stretching strains.

Computations for the out-of-plane shear behaviour relation, $\bar{\sigma}_{12}(\varepsilon_{12}^{\mathrm{p}})/\bar{\sigma}_{12}(0)$, are carried out using the same unit cell, but now with the top plate displaced in the 1- and 2-directions in such a way that the net force in the 2-direction vanishes. Periodicity conditions are imposed on the edges of the web in the cell. The nominal stress and overall plastic shear strain rate are converted to true stress, $\bar{\sigma}_{12}$, logarithmic strain rate, $\dot{\varepsilon}_{12}^{\mathrm{p}}$. Prior to the onset of shear buckling, the overall shear response in Figure 7(d) is essentially the normalized shear stress–strain curve of the web. The overall shear strength is only slightly eroded by shear buckling of the web (Figure 7(b)) over the range of plastic strain plotted.

Finally, results for in-plane shear have also been included in Figure 7(d) even though they are essentially irrelevant to performance of the square honeycomb core because $\bar{\sigma}_{13}(0) \cong 0.044\,\mathrm{MPa}$ is so small. These results are obtained by imposing displacements associated with the shear of the faces on the top and bottom edges of the webs of the unit core cell and computing the cell's shear resistance. Similarly, the elastic modulus governing in-plane shear is very small ($G_{13} \approx 0.0015\,\mathrm{GPa}$) compared to the other moduli and to the in-plane stiffness contribution of the face sheets.

In any application of the constitutive model, it will be necessary to identify $\sigma_0(\varepsilon_{\mathrm{ep}})$ with the dominant history for that application and then assess how good or bad this choice is for the other relevant modes of stressing. The curves in Figure 7(d) give some sense of how effective this approach will be for the square honeycomb core when $\sigma_0(\varepsilon_{\mathrm{ep}})$ is determined from either $\bar{\sigma}_{22}(\varepsilon_{11}^{\mathrm{p}})$ or $\bar{\sigma}_{12}(\varepsilon_{12}^{\mathrm{p}})$. In some instances, a better approach might be to make a choice for $\sigma_0(\varepsilon_{\mathrm{ep}})$ that provides a compromise fit to several of the basic histories. Such ambiguity is encountered in the application of any of the conventional plasticity models with a hardening function based on a single measure of plastic strain. Examples discussed in Section 5 illustrate some of the issues.

4.2. Pyramidal truss core

The approach to the pyramidal truss and folded plate cores is similar to that just described for the square honeycomb core and these cases will be presented with less discussion. The unit cell of the pyramidal truss core is shown in Figure 8(a), together with the co-ordinate system. As in the case of the square honeycomb, the 1- and 3-directions can be interchanged due to symmetry. The ends of the truss members are welded to face sheets that permit no

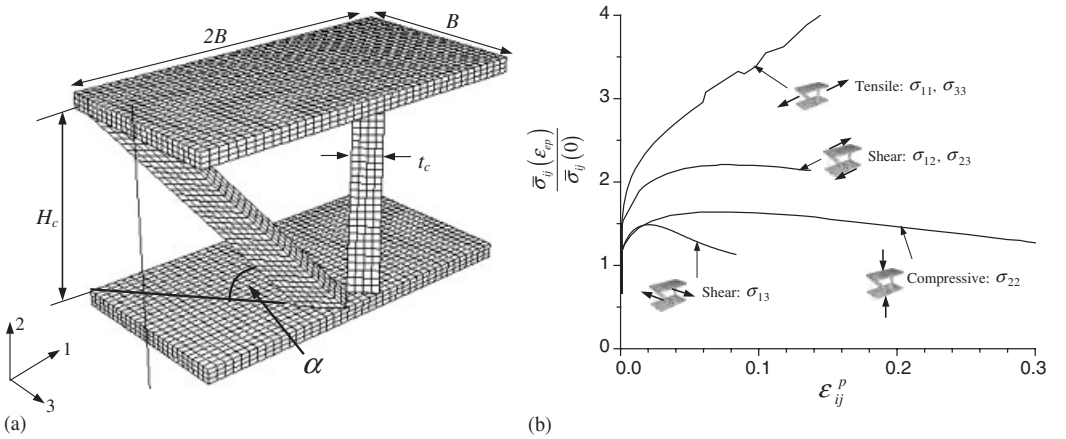

Figure 8. (a) Finite element model of a unit core cell for pyramidal truss core geometry; and (b) normalized stress–plastic strain relationships for pyramidal truss core.

rotation of the ends of the truss members. Each truss member has a solid square cross-section of width t_c. The height of the core is H_c and the inclination angle of each member is α. The cell half-width, B, is given by

$$B = (t_c + t_c/\sin\alpha + H_c/\tan\alpha)/\sqrt{2} \tag{32}$$

and the relative density of core, $\bar{\rho}_c$, is

$$\bar{\rho}_c = \frac{2t_c^2}{(t_c + t_c/\sin\alpha + H_c/\tan\alpha)^2 \sin\alpha} \tag{33}$$

In the calculations, the specific core element considered has $\alpha = 45°$, $t_c/H_c = 0.167$, corresponding to $B/H_c = 0.992$ and $\bar{\rho}_c = 0.04$.

Elementary theoretical analysis gives

$$\bar{\sigma}_{22}(0) = \sigma_Y \bar{\rho}_c \sin^2\alpha = 4.1\,\text{MPa}, \quad \bar{\sigma}_{12}(0) = \bar{\sigma}_{23}(0) = \frac{1}{2\sqrt{2}}\sigma_Y \bar{\rho}_c \sin 2\alpha = 2.90\,\text{MPa} \tag{34a}$$

$$E_{22} = E\bar{\rho}_c \sin^4\alpha = 2\,\text{GPa}, \quad G_{12} = G_{23} = \tfrac{1}{8} E\bar{\rho}_c \sin^2 2\alpha = 1\,\text{GPa} \tag{34b}$$

where terms of relative order t_c/H_c are neglected and the numerical values are for the specific example cited above. The in-plane strength and stiffness of the truss core are exceptional small and of little consequence. For the specific numerical case cited, $\bar{\sigma}_{11}(0) = \bar{\sigma}_{33}(0) \approx 0.28\,\text{MPa}$, $\bar{\sigma}_{13}(0) \approx 0.26\,\text{MPa}$, $E_1 = E_3 \approx 0.092\,\text{GPa}$ and $G_{13} \approx 0.1\,\text{GPa}$. The Poisson ratios in the elastic and plastic ranges are again taken to be zero.

Finite element simulations have been also performed to calibrate all basic stress histories of the pyramidal truss core following the same procedures discussed in Section 4.1.2. The curves for the histories of normalized stress as a function of plastic strain are plotted in Figure 8(b). As already emphasized the results for in-plane stretch and shear are of little consequence

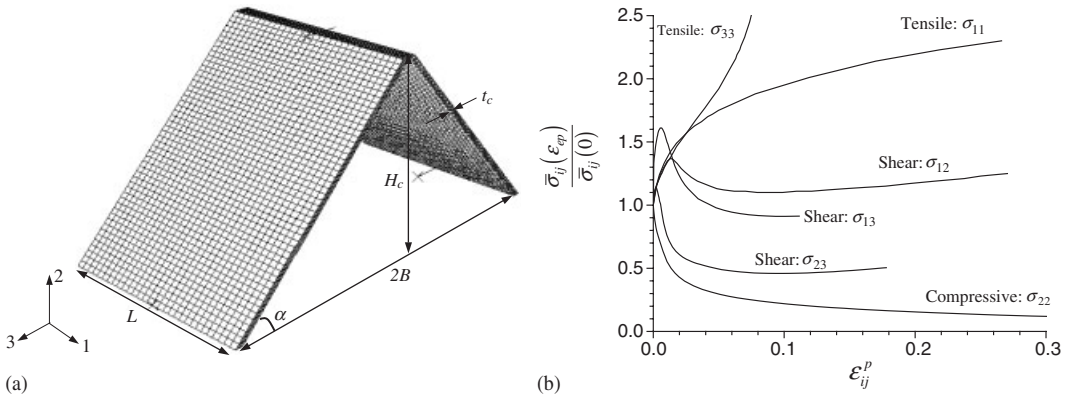

Figure 9. (a) Finite element model of a unit core cell for folded plate core geometry; and (b) normalized stress–plastic strain relationships for folded plate core.

for the truss core since the associated strengths and stiffnesses are so low. For out-of-plane compression, $\bar{\sigma}_{22}$, the truss members undergo buckling in the plastic range but they retain most of their load carrying capability following buckling due to the high strain hardening of the material and the relative stubbiness of the members. Similarly, in shear, $\bar{\sigma}_{12}$, half of the members buckle in the plastic range without much erosion of strength in the range of strain shown. While the effective stress–plastic strain curves governing out-of-plane crushing and shear are by no means coincident, they are nevertheless sufficiently similar that choice of the hardening function for the continuum constitutive model is not likely to be a complicated task in this case.

4.3. Folded plate core

A segment of length L of the folded plate core is shown in Figure 9(a) along with the co-ordinate system. This core has full orthotropic anisotropy. In particular, the in-plane stretching stiffness and strength are substantial in the 1-direction but negligible in the 3-direction. The core plate has core height H_c, core plate thickness t_c, and core inclination angle α. The unit cell size B is given by

$$B = t_c/\sin\alpha + H_c/\tan\alpha \tag{35}$$

and the relative density of core, $\bar{\rho}_c$, is

$$\bar{\rho}_c = \frac{t_c}{t_c + H_c \cdot \cos\alpha} \tag{36}$$

In the calculations, we consider the core element with a set of specified values of $\alpha = 45°$, $t_c/H_c = 0.0295$, corresponding to $B_c/H_c = 1.042$ and $\bar{\rho}_c = 0.04$.

For the folded plate core with full orthotropic anisotropy all six basic histories must be considered in calibrating the continuum constitutive model. Theoretical analysis gives

$$\bar{\sigma}_{11}(0) = \sigma_Y \bar{\rho}_c = 8.2\,\text{MPa}, \quad \bar{\sigma}_{22}(0) = \sigma_Y \bar{\rho}_c \sin^2\alpha = 4.1\,\text{MPa} \tag{37a}$$

$$\bar{\sigma}_{12}(0) = \tau_Y \bar{\rho}_c \sin\alpha = 3.35\ \text{MPa}, \quad \bar{\sigma}_{23}(0) = \tfrac{1}{2}\sigma_Y \bar{\rho}_c \sin 2\alpha = 4.1\ \text{MPa}$$

$$\bar{\sigma}_{13}(0) = \tau_Y \bar{\rho}_c \cos\alpha = 3.35\ \text{MPa} \tag{37b}$$

$$E_{11} = E\bar{\rho}_c = 8\ \text{GPa}, \quad E_{22} = E\bar{\rho}_c \sin^4\alpha = 2\ \text{GPa} \tag{37c}$$

$$G_{12} = G\bar{\rho}_c \sin^2\alpha = 1.54\ \text{GPa}, \quad G_{23} = \tfrac{1}{4} E\bar{\rho}_c \sin^2 2\alpha = 2\ \text{GPa}$$

$$G_{13} = \tfrac{1}{2} G\bar{\rho}_c \sin 2\alpha = 1.54\ \text{GPa} \tag{37d}$$

where terms of relative order t_c/H_c are neglected and the numerical values correspond to the specific case for which computed results are presented. The in-plane modulus and strength in the 3-direction are both very small and inconsequential, i.e. $E_{33} \approx 0.0041$ GPa and $\bar{\sigma}_{33}(0) \approx 0.1$ MPa for the numerical example. Elastic and plastic Poisson ratios are again taken to be zero.

The basic stress histories for the folded plate core where computed by imposing conditions along the top and bottom edges of the segment in Figure 9(a) consistent with attachment to rigid face sheets as described for the square honeycomb. Periodicity conditions were imposed on the segment ends. The computed stress–plastic strain curves for the basic histories, each normalized by the associated initial yield stress above, are plotted in Figure 9(b). For $\bar{\sigma}_{12}(\varepsilon^p_{12})$ and $\bar{\sigma}_{23}(\varepsilon^p_{23})$, the response subsequent to buckling depends on the length of the segment, L, and computations were performed over a range of L. The curves shown in Figure 9(b) correspond to the segment length producing the lowest curve for that case. Each of the basic histories in Figure 9(b) is significant except that for stressing in the 3-direction, $\bar{\sigma}_{33}$. While substantial, the response for in-plane shearing, $\bar{\sigma}_{13}(\varepsilon^p_{13})$, is not likely to play an very important role in the response of a sandwich plate since the face sheets usually supply ample in-plane shear stiffness and strength. The curve for tension in the 1-direction is essentially the tensile stress–strain curve of the material, and it has been terminated at the point that necking sets in. Plastic buckling of the webs for out-of-plane compression and for each of the three shear stressing histories leads to significant softening behaviour with increasing effective plastic strain. The rapid erosion of strength due to buckling is particularly notable for out-of-plane compression, $\bar{\sigma}_{22}$. The web is relatively slender falling in the range where elastic buckling and plastic yielding are almost coincident. It will be seen in the next section that such dramatic softening behaviour presents difficulties in modelling the core with a continuum model.

5. SANDWICH PLATES SUBJECT TO UNIFORM STATIC PRESSURE: FULL THREE-DIMENSIONAL SIMULATIONS AND RESULTS BASED ON THE CONTINUUM CONSTITUTIVE MODEL OF THE CORE

Xue and Hutchinson [3] have employed three-dimensional finite element modelling of sandwich plates to investigate their performance under static and dynamic loading where the core members were fully meshed. In this section, similar three-dimensional simulations will be presented and compared with results based on the continuum model of the core to provide an assessment of the validity of the latter approach. Comparisons for each of the three core types considered in the last section will be made. Infinite plates of width $2L$ that are clamped along their edges

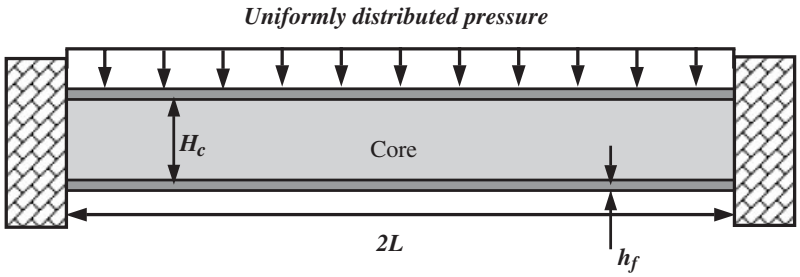

Figure 10. Clamped sandwich plate subject to uniform static pressure load.

are considered, as depicted in Figure 10. The plates have face sheet thickness of h_f and core height H_c. A uniformly distributed pressure, p, is applied statically to the top surface of the plates. The details of the finite element modelling with full meshing of the core members have been described and illustrated in the previous paper. The finite element model is fully three-dimensional with detailed meshing of the core members, and it exploits periodicity of the plate in its long direction. The reader is referred to Reference [3] for details of these calculations.

In the representative examples considered below, each of the three sandwich plates has a core with relative density, $\bar{\rho}_c = 0.04$, normalized core height, $H_c/L = 0.1$ and normalized face sheet thickness, $h_f/H_c = 0.08$. The three sandwich plates have the same total mass, each with a core mass constituting 20% of the total. The tensile stress–strain behaviour of material in the plates is taken to be (22). In both sets of calculations, the faces are modelled by the Mises yield surface, as are the core members in the full three-dimensional simulations. In each of calculations employing the continuum model of the core, $\sigma_0(\varepsilon_{ep})$ is determined either directly from $\bar{\sigma}_{22}(\varepsilon^p_{22})$ or $\bar{\sigma}_{12}(\varepsilon^p_{12})$, or as a perfectly-plastic approximation to one of these two histories, as described below. The α's are defined using the initial yield stresses given earlier. The continuum core model enables the sandwich plate under uniform pressure in Figure 10 to be treated as a plane strain problem that is then represented by a two-dimensional finite element model. Typically, one of the full three-dimensional simulations takes at least several hours to run while the two-dimensional computation requires only several minutes on the same workstation. Even if the problem based on the continuum constitutive relation for the core were formulated as a three-dimensional problem, it would require significantly less computation time due to the fact that it requires far fewer elements in the core than simulations that mesh the full core geometry.

A reference pressure, p_c, is defined corresponding to the limit pressure in bending of a solid, clamped, elastic-perfectly plastic plate of width, $2L$, having thickness, h, yield stress, σ_Y, that is subject to a uniform static pressure:

$$p_c = \sigma_Y h^2/L^2 \tag{38}$$

Here, σ_Y is identified with the initial tensile yield stress of material (1) and $h = 2h_f + \bar{\rho}_c H_c$ is the thickness of the solid plate having the same mass per area as the sandwich plate.

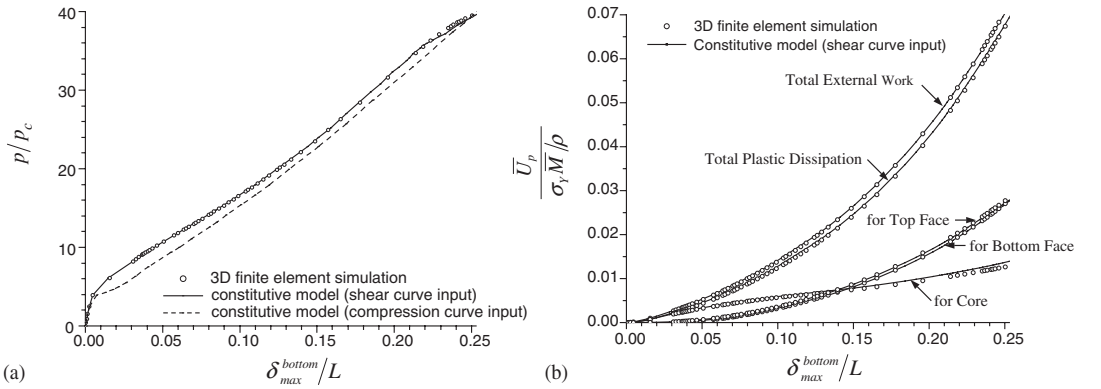

Figure 11. (a) Normalized pressure as a function of the maximum deflection of the bottom face sheet obtained from the three simulations for square honeycomb core; and (b) normalized plastic dissipation in the plate for the three-dimensional calculation and the calculation using continuum model based $\bar{\sigma}_{12}(\bar{\varepsilon}^{\mathrm{p}}_{12})$ for square honeycomb core; the difference between total external work and total plastic dissipation is elastic stored energy.

5.1. Square honeycomb core sandwich plate

Figure 11(a) presents the relation between the normalized pressure, p/p_{c}, and the normalized maximum displacement of bottom face sheet, $\delta^{\mathrm{bottom}}_{\mathrm{max}}/L$, for square honeycomb core. The hollow points are the numerical results from the full three-dimensional finite element simulation. The dimensions of the sandwich plate and its material properties are such that the core yielding in shear is the first occurrence of non-linear behaviour. The solid curve in Figure 11(a) has been determined from the continuum core modelling with $\sigma_0(\varepsilon_{\mathrm{ep}})$ determined by a fit to $\bar{\sigma}_{12}(\bar{\varepsilon}^{\mathrm{p}}_{12})$ in Figure 7(d).[¶] The agreement with the three-dimensional predictions is exceptionally good. Also included in Figure 11(a) is the prediction that employed an elastic-perfectly plastic representation of the crushing stress–strain data, $\bar{\sigma}_{22}(\bar{\varepsilon}^{\mathrm{p}}_{22})$, according to $\sigma_0(\varepsilon_{\mathrm{ep}}) = \bar{\sigma}_{22}(0)$. Initial yield of the sandwich plate at $p/p_{\mathrm{c}} \approx 4$ is still accurately captured since the continuum model of the core reproduces the initial yield stresses for each of the basic stress histories. However, the core in calculation based on the choice $\sigma_0(\varepsilon_{\mathrm{ep}}) = \bar{\sigma}_{22}(0)$ does not have the strong strain hardening that the shear behaviour displays, and consequently the corresponding response of the sandwich plate in Figure 11(a) falls below the other two results. Nevertheless, the discrepancy is small except in the earliest stages of plastic deformation. At larger deflections of the plate, in-plane stretching becomes dominant and the discrepancy recedes. In overall stretching, the results are not highly sensitive to the details of the square honeycomb core representation since approximately 90% of the stretching strength is contributed by the face sheets (e.g. the core constitutes 20% of the total mass and only one half of the core webs are aligned in the stretching direction).

[¶]When the basic stress history to be used for the determination of $\sigma_0(\varepsilon_{\mathrm{ep}})$ has been identified, $\sigma_0(0)$ is then established. Note that $\sigma_0(0)$ is involved in the evaluation of α_{ij} through its role in the definition of R_{ij}, and, accordingly, the choice of $\sigma_0(0)$ is involved in the definition of $\varepsilon_{\mathrm{ep}}$.

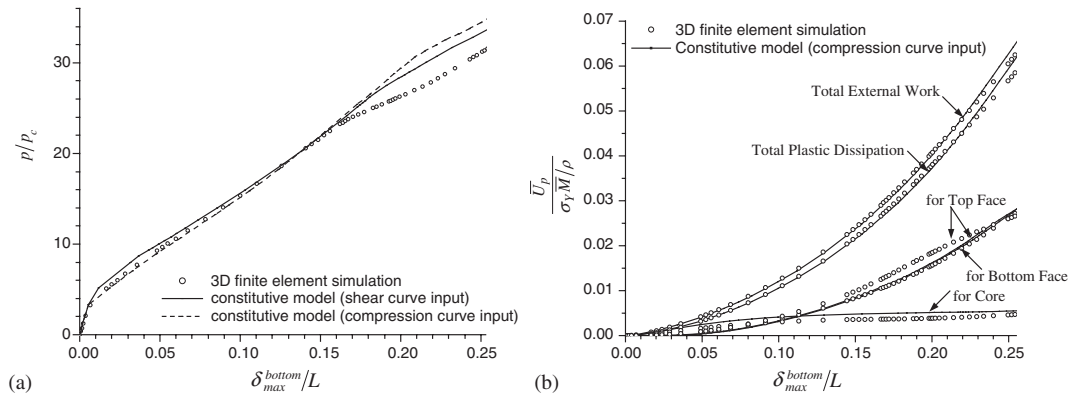

Figure 12. (a) Normalized pressure as a function of the maximum deflection of the bottom face sheet obtained from the three simulations for pyramidal truss core; and (b) normalized plastic dissipation in the plate for the three-dimensional calculation and the calculation using continuum model based $\bar{\sigma}_{22}(\bar{\varepsilon}^{\mathrm{p}}_{22})$ for pyramidal truss core; the difference between total external work and total plastic dissipation is elastic stored energy.

The plastic energy absorption per unit area averaged over the plate, $\bar{U}_{\mathrm{p}}$, for different parts of the sandwich plate as a function of the deflection of the bottom face sheet is presented as the dimensionless plot of $\bar{U}_{\mathrm{p}}/(\sigma_Y \bar{M}/\rho)$ versus $\delta^{\mathrm{bottom}}_{\mathrm{max}}/L$ in Figure 11(b), where in all the present examples $\bar{M} = 0.02\rho L$. The solid curves are based on the calculations in which the continuum core model is fit to the shear data and the open circular points are the results of the three-dimensional simulation. It is seem that the continuum approach accurately reproduces the more elaborate results in detail, not only for the overall response. The total external work of the pressure slightly exceeds the total plastic dissipation in the plate because some residual stress (and stored elastic energy) is produced. Even this detail is accurately captured by the simpler approach. Figure 11(b) reveals that nearly all the plastic dissipation occurs in the core in the early stage of deformation due to core yielding in shear. At larger deflections, when stretching becomes dominant, the faces increasingly absorb more and more of the energy, but the core webs aligned with the stretch direction also make some contribution as discussed earlier.

5.2. Pyramidal truss core sandwich plate

The process described above was repeated for the sandwich plate with the pyramidal truss core. As in the case of the honeycomb core, the dimensions of the core are such that the yielding of the core in shear is the first non-linear mechanism to occur. The effective stress–strain function of the continuum representation of the pyramidal truss core, $\sigma_0(\varepsilon_{\mathrm{ep}})$, is determined from $\bar{\sigma}_{12}(\bar{\varepsilon}^{\mathrm{p}}_{12})$ in Figure 8(b) in one set of calculations and from $\bar{\sigma}_{22}(\bar{\varepsilon}^{\mathrm{p}}_{22})$ in the other. In these calculations, the fit is made to each of the curves directly. Curves of pressure as a function of the maximum deflection of the bottom face sheet obtained from the three simulations are presented in Figure 12(a), with plots of plastic dissipation in the plate given in Figure 12(b) for the three-dimensional calculation and the calculation using continuum model based

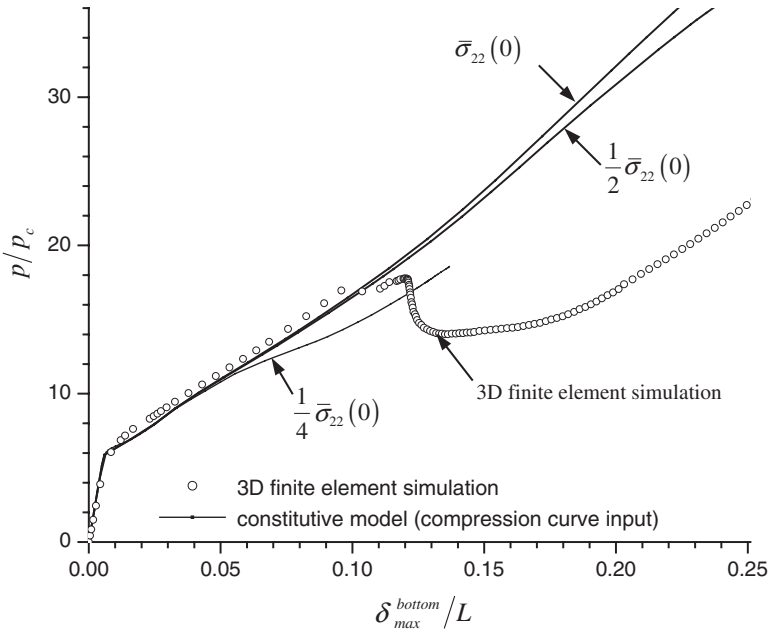

Figure 13. Normalized pressure as a function of the maximum deflection of the bottom face sheet obtained from the three simulations for folded plate core.

$\bar{\sigma}_{22}(\varepsilon_{22}^{\mathrm{p}})$. In this case, the difference between $\sigma_0(\varepsilon_{\mathrm{ep}})$ as determined by $\bar{\sigma}_{22}(\varepsilon_{22}^{\mathrm{p}})$ or $\bar{\sigma}_{12}(\varepsilon_{12}^{\mathrm{p}})$ is not nearly as large as for the honeycomb core, and this is reflected by the close agreement between the two sets of continuum core model predictions in Figure 12(a). The agreement with the three-dimensional results is very close until deflections as large as $\delta_{\max}^{\mathrm{bottom}}/L \approx 0.15$. Both results based on the continuum representation of the core significantly overestimate the stretching strength of the core, which is negligible, and this accounts for the divergence from the three-dimensional results at large deflections when stretching dominates. The fact that the discrepancy is not greater is due to the fact that the core only constitutes 20% of the total mass and thus, at the most, could not contribute more than 20% of the stretching strength of the plate. The plot of energy dissipation in Figure 12(b) is consistent with these remarks.

5.3. Folded plate core sandwich plate

The basic stress–strain histories of the folded plate core in Figure 9(b) are highly disparate due to the various modes of plastic buckling of the core webs. The compression curve, $\bar{\sigma}_{22}(\varepsilon_{22}^{\mathrm{p}})$, falls sharply with yielding and buckling. The unusually low post-buckling strength of the folded plate core may limit its utility. Comparisons between the three-dimensional analysis and the plane strain analysis based on the continuum core constitutive model are shown in Figure 13. We have not attempted to fit the constitutive model directly to any of the basic stress histories in Figure 9(b) since that would almost certainly cause numerical problems due to the extreme softening response. Instead, the model was taken to be elastic perfectly plastic (i.e. $\sigma_0(\varepsilon_{\mathrm{ep}})$ was

constant). The elastic moduli and initial yield stresses were fit to the values listed in Equation (37). The predictions based on this choice are plotted as the upper solid curve labelled as $\bar{\sigma}_{22}(0)$ in Figure 13. The curves labelled $\frac{1}{2}\,\bar{\sigma}_{22}(0)$ and $\frac{1}{4}\,\bar{\sigma}_{22}(0)$ in Figure 13 are computed in the same manner except that now the initial yield stress for uniaxial stressing in the 2-direction is taken to be one half and one quarter, respectively, that of the previous calculation with all the other initial yield stress components unchanged. The continuum core approach reproduces the three-dimensional simulation for $\delta_{\max}^{\text{bottom}} < 0.13$, but fails to capture the dramatic drop in load carrying capacity at larger deflections. In the range of lower deflections yielding is dominated by shear yielding (σ_{12}) in the core. The constitutive model adequately replicates the sandwich plate behaviour because each of the initial yield stresses of the basic histories is accurately reproduced. The drop in load for $\delta_{\max}^{\text{bottom}} > 0.13$ seen for the three-dimensional simulation involves buckling of the core webs under a combination of shear and compression. The continuum constitutive model for the folded plate core is not able to reproduce this behaviour. A premature onset of core crushing and bending stiffness reduction occurs when the yield stress in crushing set to $\frac{1}{4}\,\bar{\sigma}_{22}(0)$, but the sudden drop in strength of the sandwich plate is not replicated.

6. DYNAMIC LOADING OF A SQUARE HONEYCOMB CORE SANDWICH PLATE

One of the motivations for developing the continuum model of the core is to enable the analysis of complex sandwich plate structures subject to high intensity dynamic loads. For such applications, extensions of the present constitutive model will be required to incorporate material strain rate dependence and local inertial effects in the core. Nevertheless, in this section, we illustrate by example the potential effectiveness of the continuum core model for dynamic loading of the clamped plate in Figure 9. The continuum model of the core in Section 4.1 will be used to describe the square honeycomb core in a dynamic simulation. The results will be compared with those from a dynamic three-dimensional simulation with full meshing of the core webs (Reference [3]). The sandwich plate analysed is precisely same as that in Section 4.1 with $\bar{\rho}_{\text{c}} = 0.04$, $H_{\text{c}}/L = 0.1$, $B/H_{\text{c}} = 1$ and $h_{\text{f}}/H_{\text{c}} = 0.08$, corresponding to a core mass that is 20% of the total.

In the simulation based on the continuum model of the core, the mass of the core is assumed distributed uniformly through the thickness. No material strain rate dependence is taken into account in either the two- or three-dimensional simulation. For the continuum representation of the core, the function $\sigma_0(\varepsilon_{\text{ep}})$ was determined by fitting to $\bar{\sigma}_{12}(\varepsilon_{12}^{\text{p}})$ in Figure 7(d). An impulsive load is applied to the top face of the plate modelling the effect of a pressure pulse whose time period is brief compared to the response time of the plate. A uniform momentum impulse per unit area I is applied to the top face sheet at the start of the simulation, corresponding to a uniform initial velocity $v = I/\rho h_{\text{f}}$ of the face.

Computations for maximum deflection of sandwich plates were carried out at difference levels of dynamic loading as measured by the normalized impulse $I/(\bar{M}\sqrt{\sigma_Y/\rho})$. Figure 14 presents the normalized final maximum deflection of sandwich plate on the top and bottom face as a function of the normalized impulse as computed by the two simulation methods. The agreement between the two sets of predictions is remarkably good. Perhaps this is not surprising, given the exceptional agreement demonstrated for the quasi-static loading in Figure 11(a). However, the impulsive loading produces considerably more core crushing than the

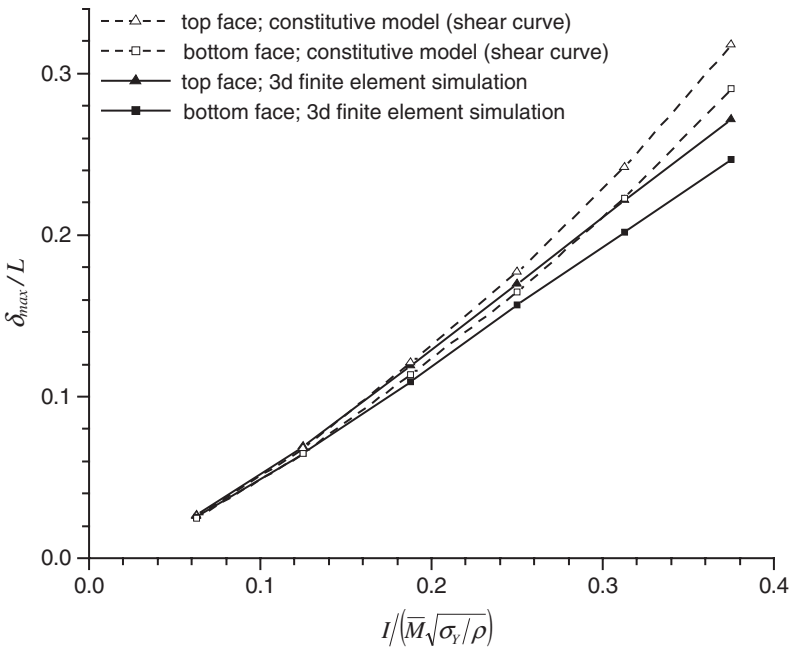

Figure 14. Normalized maximum deflection of the top and bottom faces of square honeycomb core sandwich plate as a function of the normalized impulse as computed by the two simulation methods.

quasi-static loading at the higher intensity impulses, as evident from the larger deflection of the top face compared to the bottom face. At the highest impulse levels in Figure 14, the crushing strain reaches almost 20%. Strain hardening in quasi-static crushing has been substantially overestimated in the continuum model of the core because $\sigma_0(\varepsilon_{ep})$ has been fit to the shear stress–strain curve. Nevertheless, at high impulses, the calculation based on the continuum model of the core indicates larger deflections of both face sheets than the more detailed three-dimensional calculation. This discrepancy is thought to be primarily a consequence of a significant enhancement of the effective crushing strength of the core under dynamic conditions arising from local inertial stabilization of the core webs [16]. The three-dimensional calculation accounts for this effect while the continuum-based approach does not. As noted above, neither set of calculations accounts for material rate dependence.

7. CONCLUSIONS

A generalization of the classical quadratic yield surface for solids with orthotropic anisotropy has been developed accounting for plastic compressibility representative of low-density metal cores structures for sandwich plates. The constitutive model permits a user to set six initial yield strengths for uniaxial and shear stressing in the three principal material directions. Selected plastic Poisson ratios governing transverse plastic strains under uniaxial stressing can also be set which are related to the plastic compressibility of the material. Equations for coefficients

of the yield function are also given in terms of these user-defined quantities. Like the classical model, the generalization invokes uniform strain hardening in which the yield surface expands or contracts uniformly and an effective plastic strain measure. The new constitutive relation has been implemented as material subroutine with ABAQUS. Selected examples have been analysed and presented to demonstrate both the robustness of the new model in a computational setting and physical aspects for sandwich plates stemming from both anisotropy and plastic compressibility.

In this paper, it has been assumed that the material comprising the core structure has sufficient ductility to withstand fracture, and calculations are carried out to large deflections. The approach has been explored for quasi-static deformations, although one example has been presented that indicates it, or a version modified to account for rate-dependent effects, is likely to be effective under high intensity dynamic loads. While all six of the initial yield stresses can be chosen by the user, the hardening function can be fit to only one of the basic histories. For sandwich plates subject to large deflections, depending on the dimensions, material properties and loading, the core may be subject to deformation involving combinations of core crushing, out-of-plane shear and in-plane stretching. The accuracy of the present constitutive model, or any other in such applications, depends on the ability of the model to approximate the relevant multi-axial responses of the core. Comparisons presented here based on three-dimensional computations with full meshing of the core geometry have shown that sandwich plates with either square honeycomb or pyramidal truss cores can be modelled by the continuum approach for sandwich plates that experience combinations of crush, shear and in-plane stretch during the deformation history. The approach can also be used for folded plate cores, although important features are not captured at larger deflections. The buckling collapse of the core webs and associated dramatic softening behaviour is difficult to model. Further work to improve the representation for this class of cores is required, including more attention to influences of initial imperfections.

A competing class of constitutive models ignores interaction between stress components under multi-axial stressing by introducing an independent yield function for each component of stress that can be fit to each of the six basic stress–strain data sets. The resulting elastic region is the convex set enclosed by the resulting set of yield planes with corners and vertices. This class of models has the obvious advantage that under uni-component stressing the stress–strain curve is reproduce for each of the six basic histories.[‖] One obvious disadvantage is that the interaction of stress components in multi-axial stressing is ignored even in initial yield, and the effective yield strength may be significantly overestimated under multi-axial stressing. Potentially more serious is the inability to reflect the multi-axial weakening of the core due to web buckling. For example, a core buckled plastically in crushing is not likely to be able to then sustain the out-of-plane shear stress of a previously unstressed core, as would be predicted for this class of models. Recent experiments measuring the static or dynamic behaviours of honeycombs, foams, and other core structures of sandwich plates [17–21] provide an opportunity for comparisons with the predictive capabilities of the models.

Constitutive modelling the multi-axial large deformation behaviour of metallic sandwich core structure is complex requiring compromise and good judgment on the part of the analyst,

[‖]A systematic study with two models of this class has been carried out by Hanssen *et al.* [9] using constitutive models included in the commercial code LS-DYNA.

particularly in deciding which stress histories are relevant and the fidelity to which they must be reproduced. The present model, which extends anisotropic plasticity based on a quadratic yield surface for highly compressible materials, has both advantages and limitations compared to alternative models available at the present time based on independent yield functions for each stress component. This quandary is not so different from what has existed for years for incompressible anisotropic plastic solids, except that the range of stress–strain responses under different loadings is exceptionally large for low-density metal core structures.

APPENDIX A: BACKWARD-EULER RETURN ALGORITHM AND CONSISTENT TANGENT MODULAR MATRICES

In order to obtain unconditional stability for integration of plasticity model, the backward-Euler algorithm is usually adopted and, at the same time, the consistent tangent modulus matrix is used to improve the convergence of the overall equilibrium iterations in the Newton–Raphson method. Backward-Euler computing procedures for various existent plasticity models are available in References [22, 23]. In this section, we will briefly present derive the algorithm for the present sandwich core model.

For the purpose of finite element implementation, we adopt a squared form of the yield criterion and express it in the matrix and vector form as

$$f_2 = \sigma_e^2 - \sigma_0^2 = \tfrac{1}{2}\,\boldsymbol{\sigma}^{\mathrm{T}}\mathbf{P}\boldsymbol{\sigma} - \sigma_0^2 = 0 \tag{A1}$$

First, we define the flow vector, $\mathbf{a}$, and the matrix $\partial\mathbf{a}/\partial\boldsymbol{\sigma}$:

$$\mathbf{a} = \frac{\partial f_2}{\partial \boldsymbol{\sigma}} = \mathbf{P}\boldsymbol{\sigma} \tag{A2}$$

$$\frac{\partial \mathbf{a}}{\partial \boldsymbol{\sigma}} = \mathbf{P} \tag{A3}$$

The plastic strain rate $\dot{\boldsymbol{\varepsilon}}_{\mathrm{p}}$ is then given by

$$\dot{\boldsymbol{\varepsilon}}_{\mathrm{p}} = [\ \dot{\varepsilon}^{\mathrm{p}}_{11}\ \dot{\varepsilon}^{\mathrm{p}}_{22}\ \dot{\varepsilon}^{\mathrm{p}}_{33}\ 2\dot{\varepsilon}^{\mathrm{p}}_{12}\ 2\dot{\varepsilon}^{\mathrm{p}}_{23}\ 2\dot{\varepsilon}^{\mathrm{p}}_{31}\ ]^{\mathrm{T}} = \dot{\lambda}_2 \frac{\partial f_2}{\partial \boldsymbol{\sigma}} = \dot{\lambda}_2 \mathbf{a} \tag{A4}$$

Compared with Equations (8) and (11), we must have

$$\dot{\varepsilon}_{\mathrm{ep}} = \dot{\lambda} = 2\sigma_e \dot{\lambda}_2 \tag{A5}$$

From Equation (14), the elastic stresses and strains are connected by

$$\boldsymbol{\sigma} = \mathbf{C}\boldsymbol{\varepsilon} \tag{A6}$$

The backward-Euler return algorithm is based on the following equation:

$$\boldsymbol{\sigma}_{\mathrm{C}} = \boldsymbol{\sigma}_{\mathrm{B}} - \mathbf{C}\Delta\boldsymbol{\varepsilon}_{\mathrm{P}} = \boldsymbol{\sigma}_{\mathrm{B}} - \Delta\lambda_2 \mathbf{C}\mathbf{a}_{\mathrm{C}} \tag{A7}$$

where $\boldsymbol{\sigma}_{\mathrm{B}}$ are the predictor stresses, and $\boldsymbol{\sigma}_{\mathrm{C}}$ are the final stresses on the yield surface. Generally, the starting estimation will not satisfy the yield function and further iterations will be required.

In order to derive such an iterative loop, a residual vector, $\mathbf{r}$, is introduced

$$\mathbf{r} = \boldsymbol{\sigma}_{\mathrm{C}} - (\boldsymbol{\sigma}_{\mathrm{B}} - \Delta\lambda_2 \mathbf{C}\mathbf{a}_{\mathrm{C}}) \tag{A8}$$

and the iterations are performed to reduce $\mathbf{r}$ to zero while the final stresses satisfy the yield criterion, $f_2 = 0$. With $\boldsymbol{\sigma}_{\mathrm{B}}$ being fixed, a truncated Taylor expansion is applied to (A8) to produce a new residual, $\mathbf{r}_{\mathrm{n}}$,

$$\mathbf{r}_{\mathrm{n}} = \mathbf{r}_0 + \dot{\boldsymbol{\sigma}}_{\mathrm{C}} + \Delta\dot{\lambda}_2 \mathbf{C}\mathbf{a}_{\mathrm{C}} + \Delta\lambda_2 \mathbf{C} \left.\frac{\partial \mathbf{a}}{\partial \boldsymbol{\sigma}}\right|_{\mathrm{C}} \dot{\boldsymbol{\sigma}}_{\mathrm{C}} \tag{A9}$$

where $\dot{\boldsymbol{\sigma}}_{\mathrm{C}}$ are the change in $\boldsymbol{\sigma}_{\mathrm{C}}$ and $\Delta\dot{\lambda}_2$ is the change in $\Delta\lambda_2$. Setting $\mathbf{r}_{\mathrm{n}}$ to zero gives

$$\dot{\boldsymbol{\sigma}}_{\mathrm{C}} = -\left(\mathbf{I} + \Delta\lambda_2 \mathbf{C} \left.\frac{\partial \mathbf{a}}{\partial \boldsymbol{\sigma}}\right|_{\mathrm{C}}\right)^{-1} (\mathbf{r}_0 + \Delta\dot{\lambda}_2 \mathbf{C}\mathbf{a}_{\mathrm{C}}) = -\mathbf{Q}\mathbf{r}_0 - \Delta\dot{\lambda}_2 \mathbf{Q}\mathbf{C}\mathbf{a}_{\mathrm{C}} \tag{A10}$$

Also, a truncated Taylor series on the yield function (A1) gives

$$f_{2\mathrm{n}} = f_{2\mathrm{o}} + \frac{\partial f_2}{\partial \boldsymbol{\sigma}} \dot{\boldsymbol{\sigma}} + \frac{\partial f_2}{\partial \varepsilon_{\mathrm{ep}}} \dot{\varepsilon}_{\mathrm{ep}} = f_{2\mathrm{o}} + \mathbf{a}_{\mathrm{C}}^{\mathrm{T}} \dot{\boldsymbol{\sigma}}_{\mathrm{C}} - 4\sigma_0 \sigma_{\mathrm{e}} H \Delta\dot{\lambda}_2 \tag{A11}$$

Substituting (A10) into (A11) and setting $f_{2\mathrm{n}}$ to zero gives

$$\Delta\dot{\lambda}_2 = \frac{f_{2\mathrm{o}} - \mathbf{a}_{\mathrm{C}}^{\mathrm{T}} \mathbf{Q}\mathbf{r}_0}{\mathbf{a}_{\mathrm{C}}^{\mathrm{T}} \mathbf{Q}\mathbf{C}\mathbf{a}_{\mathrm{C}} + 4\sigma_0 \sigma_{\mathrm{e}} H} \tag{A12}$$

Consequently, the iterative stress change $\dot{\boldsymbol{\sigma}}_{\mathrm{C}}$ can be obtained from (A10) and also, the iterative change in the equivalent plastic strain is $\Delta\dot{\varepsilon}_{\mathrm{ep}} = 2\sigma_{\mathrm{e}} \Delta\dot{\lambda}_2$.

The consistent tangent modular matrix can be derived from the differentiation of (A8) as

$$\dot{\boldsymbol{\sigma}} = \left(\mathbf{I} + \Delta\lambda_2 \mathbf{C} \frac{\partial \mathbf{a}}{\partial \boldsymbol{\sigma}}\right)^{-1} \mathbf{C}(\dot{\boldsymbol{\varepsilon}} - \Delta\dot{\lambda}_2 \mathbf{a}) = \mathbf{R}(\dot{\boldsymbol{\varepsilon}} - \Delta\dot{\lambda}_2 \mathbf{a}) \tag{A13}$$

To remain on the yield surface, $\dot{f}_2$ should be zero, hence from (A11) and (A13),

$$\Delta\dot{\lambda}_2 = \frac{\mathbf{a}^{\mathrm{T}} \mathbf{R} \dot{\boldsymbol{\varepsilon}}}{\mathbf{a}^{\mathrm{T}} \mathbf{R}\mathbf{a} + 4\sigma_0 \sigma_{\mathrm{e}} H} \tag{A14}$$

Substituting (A14) into (A13), we obtain the consistent tangent modular matrix $\mathbf{C}_{\mathrm{ct}}$

$$\dot{\boldsymbol{\sigma}} = \mathbf{C}_{\mathrm{ct}} \dot{\boldsymbol{\varepsilon}} = \left(\mathbf{R} - \frac{\mathbf{R}\mathbf{a}\mathbf{a}^{\mathrm{T}}\mathbf{R}}{\mathbf{a}^{\mathrm{T}} \mathbf{R}\mathbf{a} + 4\sigma_0 \sigma_{\mathrm{e}} H}\right) \dot{\boldsymbol{\varepsilon}} \tag{A15}$$

The programming flow diagram based on the above algorithm for the present constitutive model is illustrated in Figure A1.

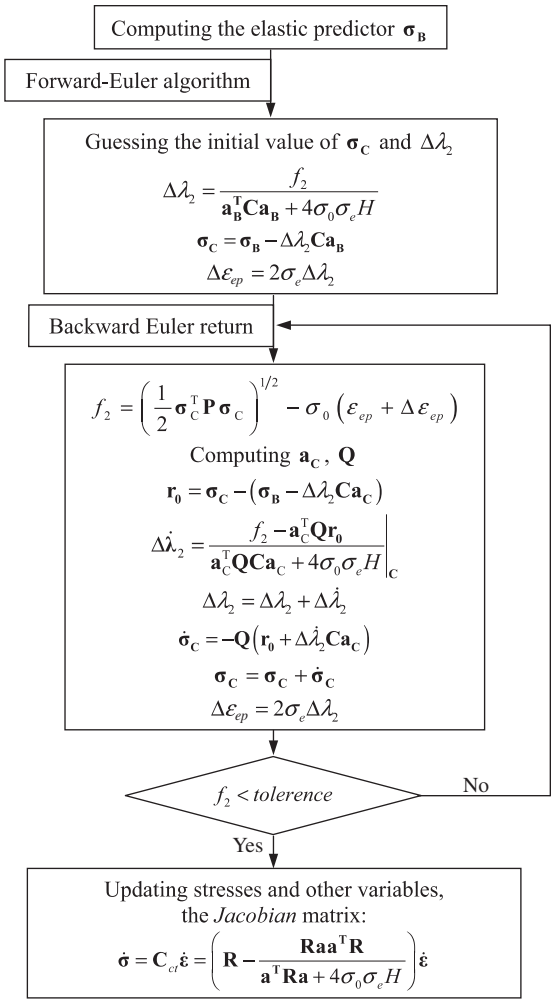

Figure A1. The programming flow diagram of the backward-Euler return algorithm for the present core model.

ACKNOWLEDGEMENTS

This work has been supported in part by the ONR under grants GG10376-114934 and N00014-02-1-0700 and in part by the Division of Engineering and Applied Sciences, Harvard University.

REFERENCES

1. Ashby MF, Evans AG, Fleck NA, Gibson LJ, Hutchinson JW, Wadley HNG. *Metal Foams*: *A Design Guide*. Butterworth-Heinemann: London, 2000.
2. Evans AG. Lightweight materials and structures. *MRS Bulletin* 2001; **26**:790–797.

3. Xue Z, Hutchinson JW. A comparative study of impulse-resistant metal sandwich plates. *International Journal of Impact Engineering* 2004; to be published.
4. Fleck NA, Deshpande VS. The resistance of clamped sandwich beams to shock loading. *Journal of Applied Mechanics* 2004; **71**:386–401.
5. Xue Z, Hutchinson JW. Preliminary assessment of sandwich plates subject to blast loads. *International Journal of Mechanical Sciences* 2003; **45**:687–705.
6. Deshpande VS, Fleck NA. Isotropic constitutive models for metallic foams. *Journal of the Mechanics and Physics of Solids* 2000; **48**:1253–1283.
7. Hill R. *The Mathematical Theory of Plasticity*. Oxford University Press: Oxford, 1950.
8. Hill R. A theory of the yielding and plastic flow of anisotropic materials. *Proceedings of Royal Society* 1947; **A193**:281–297.
9. Hanssen AG, Langseth M, Hopperstad OS. Crush behaviour of foam-based components: validation of numerical simulations. *Advanced Engineering Materials* 2002; **4**:771–776.
10. ABAQUS/Standard User's Manual, Version 6.0, Hibbit, Karlsson and Sorensen Inc.: 2001.
11. Boyer HE, Gall TL. *Metals Handbook Desk Edition*, American Society for Metals: Metals Park, OH, 1985.
12. Lubliner J. *Plasticity Theory*. Macmillan Publishing Company: New York, 1990.
13. McMeeking RM. Work in progress, private communication.
14. He M-Y, Evans AG. Work in progress, private communication.
15. Cote F, Desphande VS, Fleck NA, Evans AG. The out-of-plane compressive behaviour of metallic honeycombs. *Materials Science and Engineering* 2004, to be published.
16. Vaughn D, Canning JM, Hutchinson JW. Plastic wave propagation and column buckling. *Journal of Applied Mechanics* 2004; to be published.
17. Rathbun HJ, Wei Z, He MY, Zok FW, Evans AG, Sypeck DJ, Wadley HNG. Measurements and simulations of the performance of metallic sandwich structures with a near optimal tetrahedral truss core. *Journal of Applied Mechanics* 2004; submitted for publication.
18. Yasui Y. Dynamic axial crushing of multi-layer honeycomb panels and impact tensile behaviour of the component members. *International Journal of Impact Engineering* 2000; **24**:659–671.
19. Yu JL, Wang X, Wei ZG, Wang EH. Deformation and failure mechanism of dynamically loaded sandwich beams with aluminum-foam core. *International Journal of Impact Engineering* 2003; **28**:331–347.
20. Zhao H, Gary G. Crushing behaviour of Aluminum honeycombs under impact loading. *International Journal of Impact Engineering* 1998; **21**:827–836.
21. Zok FW, Rathbun HJ, Wei Z, Evans AG. Design of metallic textile core sandwich panels. *International Journal of Solids and Structures* 2003; **40**:5707–5722.
22. Crisfield MA. *Non-linear Finite Element Analysis of Solids and Structures*, vol. 1. Wiley: West Sussex, UK, 1991.
23. Crisfield MA. *Non-linear Finite Element Analysis of Solids and Structures*, vol. 2. Wiley: West Sussex, UK, 1991.

